Meteoritics & Planetary Science 37, 1729–1755 (2002)
Available online at http://www.uark.edu/meteor

Calcium-aluminum-rich inclusions and amoeboid olivine aggregates from the CR carbonaceous chondrites

JÉRÔME ALÉON[1]*, ALEXANDER N. KROT[2] AND KEVIN D. MCKEEGAN[1]

[1]Centre de Recherches Petrographiques et Geochimiques, CNRS UPR 2300, 15 rue Notre-Dame des Pauvres, BP20, 54501 Vandoeuvre-les-Nancy, France
[2]Hawai'i Institute of Geophysics and Planetology, School of Ocean and Earth Science and Technology, University of Hawai'i, Honolulu, Hawai'i 96822, USA
*Correspondence author's e-mail address: aleon@crpg.cnrs-nancy.fr

(Received 2002 February 21; accepted in revised form 2002 August 9)

Abstract–Calcium-aluminum-rich refractory inclusions (CAIs) in CR chondrites are rare (<1 vol%), fairly small (<500 μm) and irregularly-shaped, and most of them are fragmented. Based on the mineralogy and petrography, they can be divided into grossite ± hibonite-rich, melilite-rich, and pyroxene-anorthite-rich CAIs. Other types of refractory objects include fine-grained spinel-melilite-pyroxene aggregates and amoeboid olivine aggregates (AOAs). Some of the pyroxene-anorthite-rich CAIs have igneous textures, and most melilite-rich CAIs share similarities to both the fluffy and compact type A CAIs found in CV chondrites. One major difference between these CAIs and those in CV, CM, and CO chondrites is that secondary mineral phases are rare.

In situ ion microprobe analyses of oxygen-isotopic compositions of 27 CAIs and AOAs from seven CR chondrites demonstrate that most of the CAIs are ^{16}O-rich (Δ^{17}O of hibonite, melilite, spinel, pyroxene, and anorthite < –22‰) and isotopically homogeneous within 3–4‰. Likewise, forsterite, spinel, anorthite, and pyroxene in AOAs have nearly identical, ^{16}O-rich compositions (–24‰ < Δ^{17}O < –20‰). In contrast, objects which show petrographic evidence for extensive melting are not as ^{16}O-rich (Δ^{17}O less than –18‰). Secondary alteration minerals replacing ^{16}O-rich melilite in melilite-rich CAIs plot along the terrestrial fractionation line.

Most CR CAIs and AOAs are mineralogically pristine objects that largely escaped thermal metamorphism and secondary alteration processes, which is reflected in their relatively homogeneous ^{16}O-rich compositions. It is likely that these objects (or their precursors) condensed in an ^{16}O-rich gaseous reservoir in the solar nebula. In contrast, several igneous CAIs are not very enriched in ^{16}O, probably as a result of their having melted in the presence of a relatively ^{16}O-poor nebular gas. If the precursors of these CAIs were as ^{16}O-rich as other CR CAIs, this implies either temporal excursions in the isotopic composition of the gas in the CAI-forming regions and/or radial transport of some CAI precursors into an ^{16}O-poor gas. The absence of oxygen isotope heterogeneity in the primary minerals of melilite-rich CAIs containing alteration products suggests that mineralogical alteration in CR chondrites did not affect oxygen-isotopic compositions of their CAIs.

INTRODUCTION

Calcium-aluminum-rich inclusions (CAIs) from chondritic meteorites are widely considered to represent the first objects that formed in the solar nebula (*e.g.*, Grossman, 1980; MacPherson *et al.*, 1988). The oxygen-isotopic compositions of CAIs have been studied extensively for their potential to decipher conditions of CAI formation and thus to bring insights regarding the high-temperature evolution of the earliest phases of the solar system (*e.g.*, Clayton *et al.*, 1977; Thiemens and Heidenreich, 1983; Clayton, 1993; Thiemens, 1999; Ireland and Fegley, 2000). However, the isotopic records in the best-studied CAIs (from CV chondrites) are complicated by post-crystallization isotopic exchange. The mechanism(s) and environment for this oxygen isotopic exchange are unclear; they may be related to high-temperature nebular processes involving an ^{16}O-poor gaseous reservoir (Clayton *et al.*, 1977; Yurimoto *et al.*, 1998) or to low-temperature processes associated with secondary mineralization accompanying aqueous alteration on meteorite parent bodies (*e.g.*, Young and Russell, 1998; Young *et al.*, 1999; Wasson *et al.*, 2001). One approach to attempt to see through the isotopic overprinting by secondary processes is to study CAIs from meteorite groups that are more pristine (*i.e.*, have suffered less hydrous alteration and secondary mineralization) than the CV, CM, and CO carbonaceous chondrites.

Prelude preprint MS#4776

The ion microprobe offers the possibility to study oxygen-isotopic compositions of CAIs that are rare and/or very small. Recent ion microprobe studies on a variety of CAIs from different classes of chondrites have shown that most small CAIs are isotopically homogeneous; however, different populations of CAIs exist in different meteorite groups (for review, see McKeegan and Leshin, 2001). Sparse data on CAIs from ordinary chondrites (McKeegan *et al.*, 1998) indicate oxygen-isotopic compositions similar to those of many CV CAIs, whereas CAIs from enstatite chondrites (Guan *et al.*, 2000; Fagan *et al.*, 2001), CH chondrites (Sahijpal *et al.*, 1999) and the two ungrouped metal-rich chondrites Hammadah al Hamra (HH) 237 and Queen Alexandra Range (QUE) 94411 (Krot *et al.*, 2001a) form distinctive groups differing in ^{16}O content along a line of slope =1.0 on the oxygen three-isotope graph.

Although the CR chondrites have experienced various degrees of aqueous alteration (Weisberg *et al.*, 1993), they are themselves recognized to be very pristine meteorites. However, their CAIs have been little studied and, in particular, oxygen-isotopic compositions of CR CAIs have not yet been determined owing to their rarity (Krot *et al.*, 2001b). In this study, we report ion microprobe measurements of the oxygen-isotopic compositions of 27 CAIs and other refractory objects from 7 of 16 CR chondrites that were studied for mineralogy and petrography. The primary goal is to establish the mineralogy and petrography of these CAIs and to compare the distribution of oxygen-isotopic anomalies within and among CR CAIs with those in other carbonaceous chondrite groups (CH, CB, CO, CM, CV).

ANALYTICAL PROCEDURES

Twenty-nine polished sections of 16 CR chondrites (sections AB from Acfer 087; AG from Acfer 139; 30 from Elephant Moraine (EET) 87730; 10 from EET 87747; 14 from EET 87770; 21 from EET 92041; 22, 23 from EET 92042; 7 from EET 92147; UH 154, MK from El Djouf 001; 17, 18, 21, 29, 31 from Graves Nunataks (GRA) 95229; 9, 11, 20, from MacAlpine Hills (MAC) 87320; 5, 6 from Meteorite Hills (MET) 00426; 16, 20, 26, 28 from Pecora Escarpment (PCA) 91082; 588-1 from Renazzo; MK from Temple Bay and 7, 8 from QUE 99177) were studied using optical microscopy, backscattered electron (BSE) imaging, x-ray elemental mapping, and electron probe microanalysis (EPMA). BSE images were obtained with the Zeiss DSM-962, JEOL JSM-5900LV, and LEO-1430VP scanning electron microscopes (SEM) using a 15–20 kV accelerating voltage and 1–2 nA beam current. Electron probe microanalyses were performed with a Cameca SX-50 electron microprobe at the University of Hawai'i (UH) using a 15 kV accelerating voltage, 10–20 nA beam current, beam size of about 1–2 μm and wavelength dispersive x-ray spectroscopy. For each element, counting times on both peak and background were 30 s (10 s for Na and K). Matrix effects were corrected using PAP procedures. The element detection limits with the Cameca SX-50 were (in wt%): 0.04 (K_2O), 0.07 (Cr_2O_3), 0.08 (Na_2O), and 0.09 (FeO). X-ray elemental maps with a resolution of 2–5 μm/pixel were acquired with five spectrometers of the Cameca microprobe operating at 15 kV accelerating voltage, 50–100 nA beam current and about 1–2 μm beam size. The Mg, Ca, and Al x-ray images were combined by using a red-green-blue-color scheme and ENVI software to obtain false color maps to identify all CAIs and amoeboid olivine aggregates (AOAs) larger than 5–10 μm in apparent diameter.

Oxygen-isotopic compositions were measured *in situ* with the UCLA Cameca IMS 1270 ion microprobe operated in multicollection mode (^{16}O, ^{17}O, and ^{18}O were measured simultaneously). ^{16}O and ^{18}O were measured at low mass resolving power (MRP $\approx$ 2000) using a Faraday cup (FC) and an electron multiplier (EM), respectively, while ^{17}O was measured using the axial EM at high MRP (>6000). A Cs^+ primary beam of 0.2–0.5 nA was used in projected diaphragm mode (Kohler mode). Ion probe sputter pits of ~20 μm in diameter were achieved in the first two sessions (July and September 2001); subsequent replacement of the primary aperture allowed a reduction of primary beam size to ~10 μm in the later sessions (October and December 2001). With such conditions, the count rates were typically ~3×10^7 counts per second (cps) for ^{16}O, ~1.5×10^4 cps for ^{17}O, and ~6×10^4 cps for ^{18}O. Each analysis was preceded by 3 min of pre-sputtering to remove the carbon coating, and check peak centering and sputtering conditions. Measurements consisted of 15 integration cycles of 10 s each (30 cycles were used when the primary current was low). Normal incidence electron flooding was used for charge compensation.

Oxygen-isotopic compositions are reported as per mil deviations from standard mean ocean water (SMOW) and as ^{16}O excesses relative to terrestrial samples ($\Delta^{17}O = \delta^{17}O - 0.52 \times \delta^{18}O$). Under the analytical conditions employed, the internal (1σ) precision of individual oxygen-isotopic analyses is typically better than 0.5‰ for $\delta^{18}O$ and <1‰ for $\delta^{17}O$. The instrumental mass fractionation is corrected for each session using three terrestrial standards: San Carlos olivine (Fa_{11}), 77-228 olivine (Fa_{15}), and Burma spinel ($MgAl_2O_4$). An olivine (Fa_{20}) from the Eagle Station pallasite, which falls on the slope 0.94 carbonaceous chondrite anhydrous minerals mixing line (CCAM line; Clayton and Mayeda, 1978) on a three-oxygen isotope plot, was measured to check the accuracy in $\Delta^{17}O$.

The uncertainty in correcting for instrumental mass fractionation for the analysis of a single spot of an unknown must reflect both the dispersion in multiple analyses of the standards (external reproducibility) as well as the internal precision obtained on that spot (which is dominated by counting statistics). For the standards, overall external reproducibilities (2σ of the mean) for $\delta^{18}O$, $\delta^{17}O$, and $\Delta^{17}O$ were 0.37‰, 0.43‰, and 0.38‰ for the San Carlos olivine, 1.63‰, 0.92‰, and 0.20‰ for the 77-228 olivine, and 1.13‰, 0.68‰, and

0.50‰ for the Burma spinel, respectively. The larger errors observed for $\delta^{18}O$ (compared to $\delta^{17}O$) in some cases reflects errors correlated by mass fractionation due to geometric differences and/or analyzing standards from different ion probe mounts. We cannot physically mount our standard materials in the same ion probe holder as the meteorite thin sections, resulting in an additional uncertainty. To account for these various sources of uncertainty, we have computed an error ellipse (95% confidence interval) by using all data from terrestrial standards (from various mounts) during a given analytical session. Using this external reproducibility ellipse and the internal precision of each analysis spot, a typical error ellipse was computed at a 95% confidence interval. The semi-axes of the error ellipse correspond to typical 2σ errors in $\delta^{18}O$ and $\delta^{17}O$ of approximately ±1.6‰ and ±2.0‰, respectively.

There exists a potential inaccuracy in correcting instrumental mass fractionation due to possible matrix effects; however, these are expected to be small for Fe-free samples (Simon *et al.*, 2000). Moreover, errors in the mass fractionation have no effect on $\Delta^{17}O$. The $\Delta^{17}O$ for all terrestrial standards is indistinguishable from 0‰ within 0.5‰; the measured and true values of $\Delta^{17}O$ for Eagle Station olivine are –4.49 ± 0.39‰ and –4.51‰ (Clayton and Mayeda, 1978), respectively. Due to the high accuracy of $\Delta^{17}O$ determinations on the standards, the precision in $\Delta^{17}O$ for each sample spot is largely limited by the precision in $\delta^{17}O$ measurements.

Following oxygen isotope measurements, each refractory inclusion analyzed was reexamined in BSE and secondary electron images to verify the locations of the sputtered craters and mineralogy of the phases analyzed.

RESULTS

Mineralogy and Petrography

Refractory inclusions constitute <1 vol% of CR chondrites. They are typically small (<500 μm) and irregularly shaped; many of them are fragmented. Based on the mineralogy and petrography, the refractory inclusions can be divided into grossite ± hibonite-rich, melilite-rich, pyroxene-anorthite-rich, spinel-pyroxene-melilite aggregates, and AOAs. The melilite-rich CAIs and AOAs are by far the most abundant types of refractory inclusions in the CR chondrites. Secondary minerals such as grossular, andradite, hedenbergite, wollastonite, and ferrous olivine, commonly observed in CV CAIs, are absent in the CR CAIs, though phyllosilicates and possibly nepheline and sodalite have been observed in two CAIs. The mineralogy and petrography of the refractory objects studied for oxygen isotopes are summarized in Table 1 and described below. Because they are fragmented, these CAIs cannot be directly compared to their counterparts in other chondrite groups in many cases. Therefore the usual terminology is not used here but relationships with well-known types of inclusions are shown in the discussion section and included in Table 1.

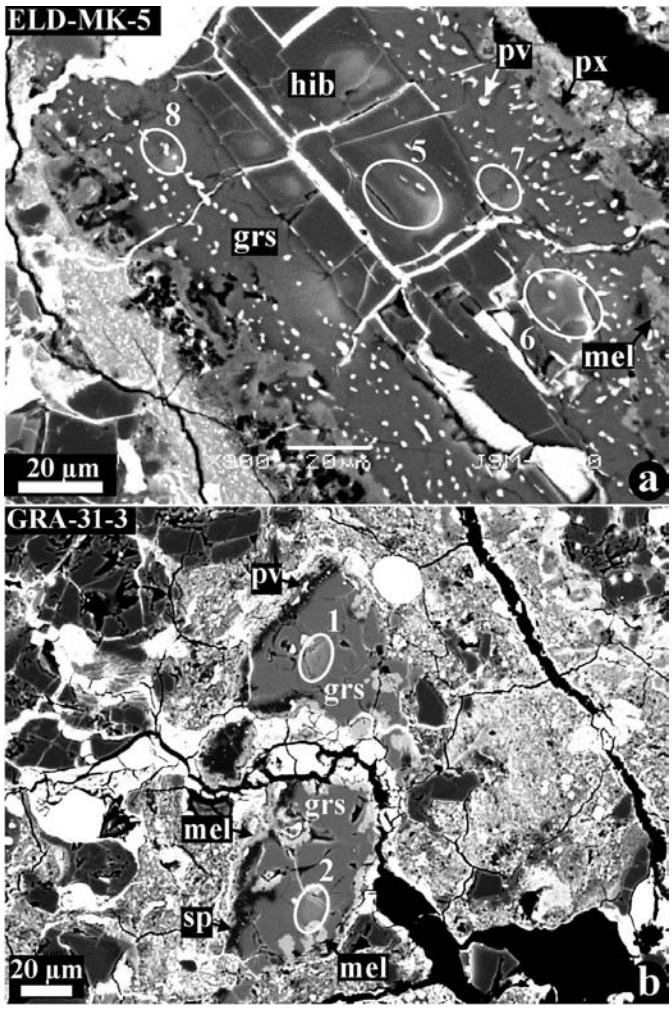

FIG. 1. BSE images of the grossite-hibonite CAI ELD-MK-5 (a) and grossite-rich CAI GRA-31-3. CAI ELD-MK-5 (a) consists of hibonite (hib) core surrounded by grossite (grs) mantle with numerous inclusions of perovksite (pv); the mantle is rimmed by melilite (mel) and pyroxene (px). Bright veins are Fe-rich products of terrestrial weathering. Here and in Figs. 2–9 ion microprobe spots produced during O-isotopic measurements are outlined; numbers near ellipsoids correspond analysis numbers listed in Table 5. Two fragments of the CAI GRA-31-3 (b) consist of grossite and minor melilite and perovskite; they are surrounded by Wark–Lovering rim layers of spinel (sp) and melilite; rare inclusions of perovskite occur in the spinel layer.

Grossite and/or Hibonite-Rich Calcium-Aluminum-Rich Inclusions–ELD-MK-5 consists of three fragments separated by matrix material (Fig. 1a). Each fragment has a hibonite core surrounded by a grossite mantle and a melilite-pyroxene rim. Grossite contains abundant inclusions of perovskite, however essentially no perovskite occurs within the hibonite. GRA-31-3 has a grossite core which contains small inclusions of melilite and perovskite (Fig. 1b). The core is rimmed by layers of spinel followed by melilite.

Melilite-Rich Calcium-Aluminum-Rich Inclusions–These CAIs consist dominantly of melilite, with abundant spinel

TABLE 1. Refractory inclusions from CR chondrites analyzed for oxygen-isotopic composition.

Sample name	Meteorite	pts	Inclusion type	Mineralogy	Comment
ELD-MK-5	El Djouf 001	MK	hib-grs-CAI	hib + grs + pv + mel [px]	–
GRA-31-3	GRA 95229	31	grs-CAI, fr	grs + mel [sp + pv + mel]	–
GRA-17-7	GRA 95229	17	mel-grs-CAI, fr	mel + sp + grs + hib [sp + mel + px]	sec, ign mel-grs
GRA-17-8	GRA 95229	17	mel-grs-CAI, fr	mel + sp + grs + hib [sp + mel + px]	sec, euh sp
GRA-18-1	GRA 95229	18	mel-CAI	mel + sp + an [px]	fl, anh sp, A
GRA-31-8	GRA 95229	31	mel-CAI	mel + sp [an + px]	anh sp, A
PCA-16-1	PCA 91082	16	mel-CAI	mel + sp + an [px + fo]	fl, anh sp, A
PCA-16-2	PCA 91082	16	mel-CAI	mel + sp + pv [mel + an + px]	anh sp, A
ELD-MK-3	El Djouf 001	MK	mel-CAI	mel + sp [px + fo]	anh sp, A
EET-21-12	EET 92041	21	mel-CAI, fr	mel + sp + pv [px]	anh sp, A
REN-588-50	Renazzo	588-1	mel-CAI	mel + sp [px]	anh sp, sec, A
EET-10-1	EET 87747	10	mel-CAI	mel + sp + pv	anh sp, A
GRA-31-2	GRA 95229	31	mel-CAI, fr	mel + sp + px + pv [px]	anh sp + sp pls, A
GRA-18-3	GRA 95229	18	mel-CAI, fr	mel + sp	euh sp, A
GRA-18-2	GRA 95229	18	mel-CAI, fr	mel + sp	euh sp, A
GRA-31-6	GRA 95229	31	FG-CAI	mel + sp + pv	–
PCA-16-3	PCA 91082	16	FG-CAI	sp + hib + pv [mel + px]	–
ELD-MK-2	El Djouf 001	MK	FG-CAI	sp + pv [mel + px]	–
EET-21-3	EET 92041	21	px-an-CAI	px + an + sp + mel + fo + mt	anh px and an, chd fr
MET-6-1	MET 00426	6	px-an-CAI, fr	an + px + mel + sp	ign
GRA-18-22	GRA 95229	18	px-an-CAI, fr	an + px + sp	ign
MET-6-2	MET 00426	6	px-an-CAI, fr	an + px + mel + sp	ign
ELD-154-10	El Djouf 001	UH 154	px-an-CAI, fr	an + px + mel + sp	ign
EET-10-3	EET 87747	10	AOA	fo + sp + an + px + mt	–
ELD-154-60	El Djouf 001	UH 154	AOA	fo + sp + an + px	–
GRA-31-10	GRA 95229	31	AOA	fo + sp + an + px	–
PCA-16-5	PCA 91082	16	AOA	fo + px + an	–

Abbreviations: pts = polished thin section; GRA = Graves Nunataks; PCA = Pecora Escarpment; EET = Elephant Moraine; MET = Meteorite Hills; CAI = calcium-aluminum-rich inclusion; AOA = amoeboid olivine aggregate; MK = M. Kilgoure; UH = University of Hawai'i; besides El Djouf 001 and Renazzo, numbers in the meteorite names are Antarctic Meteorite Working Group designations; hib = hibonite; grs = grossite; pv = perovskite; mel = melilite; sp = spinel; px = pyroxene; an = anorthite; fo = forsterite; mt = metal; sec = secondary minerals [rim minerals]; anh = anhedral; euh = euhedral; pls = palisades; fl = fluffy; chd = chondrule; ign = igneous; fr = fragment; FG = fine-grained; A = similarities with type A inclusions.

as well as anorthite in some cases; pyroxene and perovskite are minor (Figs. 2–4). Spinel grains are typically heterogeneously distributed within a CAI although one sample exhibits spinel palisades (Fig. 2b). Most spinels are anhedral and surrounded by melilite and Al-Ti-diopside, but GRA-18-3 contains euhedral spinel grains (Fig. 2c). Anorthite is a secondary mineral replacing melilite (Figs. 3c and 4). Melilite in REN-588-50 is replaced by Na- and Cl-bearing secondary phases (Fig. 5). Weisberg *et al.* (unpubl. data) tentatively identified these phases as sodalite, but that there are two secondary phases, the first Na-rich and Cl-bearing (in wt%, SiO_2, 38.9; Al_2O_3, 34.1; MgO, 6.4, CaO, 1.2, Na_2O, 6.8, K_2O, 0.27; total, 87.7; Cl has been detected in Cl Kα elemental map, but has not been analyzed) and the second Na-poor and Cl-free (in wt%, SiO_2, 38.8; Al_2O_3, 33.5; MgO, 6.2, CaO, 3.7, Na_2O, 1.9, K_2O, 0.35; total, 84.7) is clear from x-ray elemental maps (Fig. 5c,d). Although volatilization of some Na during microprobe analysis did take place, the low analytical totals of these secondary phases suggest that they are probably hydrated. The melilite-rich CAIs are typically surrounded by monomineralic pyroxene rims; pyroxene-forsterite rims are less common (Figs. 3a and 4c). Most of these CAIs share similarities with type A inclusions.

Two of the melilite-rich CAIs, GRA-17-7 and GRA-17-8, have grossite-perovskite-melilite ± hibonite mantles and may represent fragments of a single CAI with a heterogeneous distribution of spinel grains (Fig. 6). Although the boundary regions between the melilite-rich cores and grossite-rich mantles in both fragments are extensively replaced by secondary fine-grained materials, there appears to be an igneous contact between melilite and grossite. This is supported by the presence of rounded inclusions of grossite in the outermost portion of the melilite-rich cores (Fig. 6c). Due to the small grain sizes of the secondary phases, mineral identification is difficult. Based on the detail x-ray elemental mapping and microprobe analyses, several grains of apparent Ca-carbonate (in wt%, SiO_2, 0.1; Al_2O_3, 4.3; CaO, 56.1; total, 60.9) were found in GRA-17-8

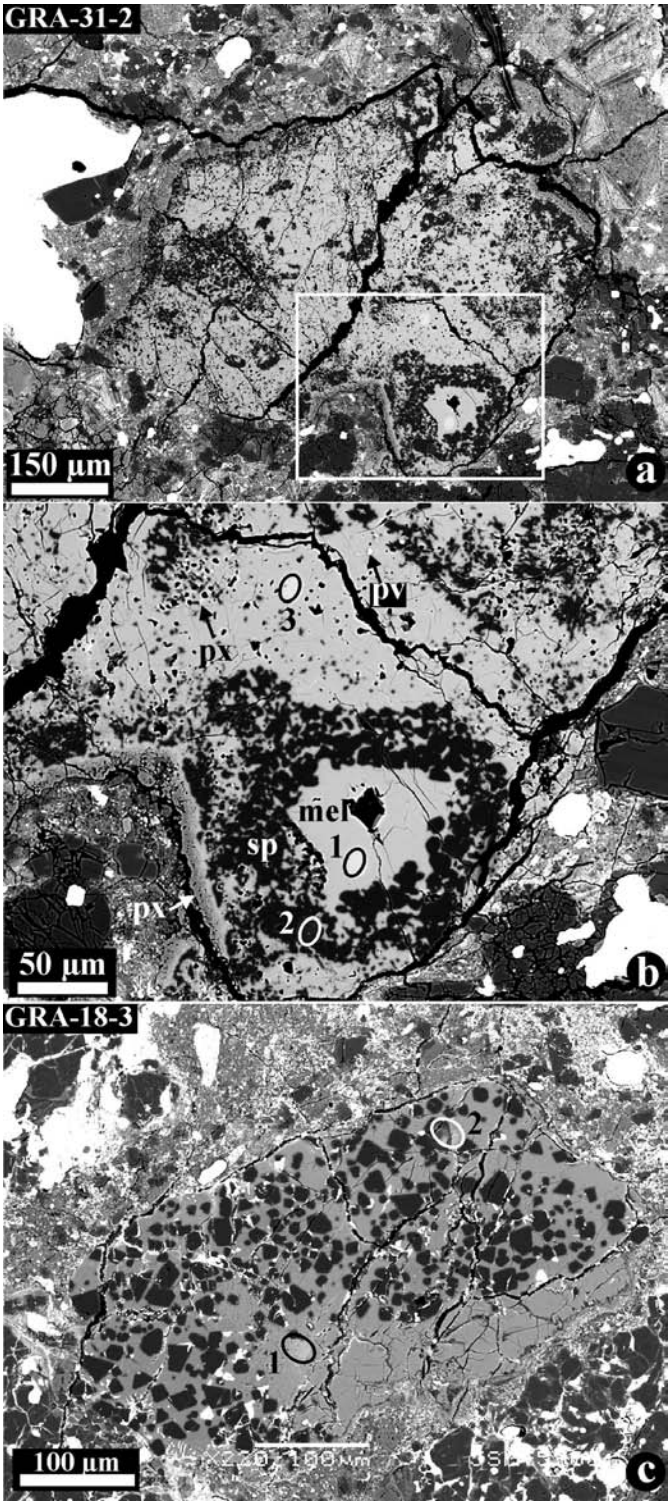

FIG. 2. BSE images of the melilite-rich CAI GRA-31-2 (a, b) and CAI fragment GRA-18-3 (d). Region outlined in (a) is shown in detail in (b). GRA-31-2 (a, b) contains rare grains of Al-Ti-diopside enclosing anhedral spinel grains and closely associated with perovskite; it also contains a spinel palisade and is rimmed by Al-diopside. Spinel grains in GRA-18-3 (c) are euhedral.

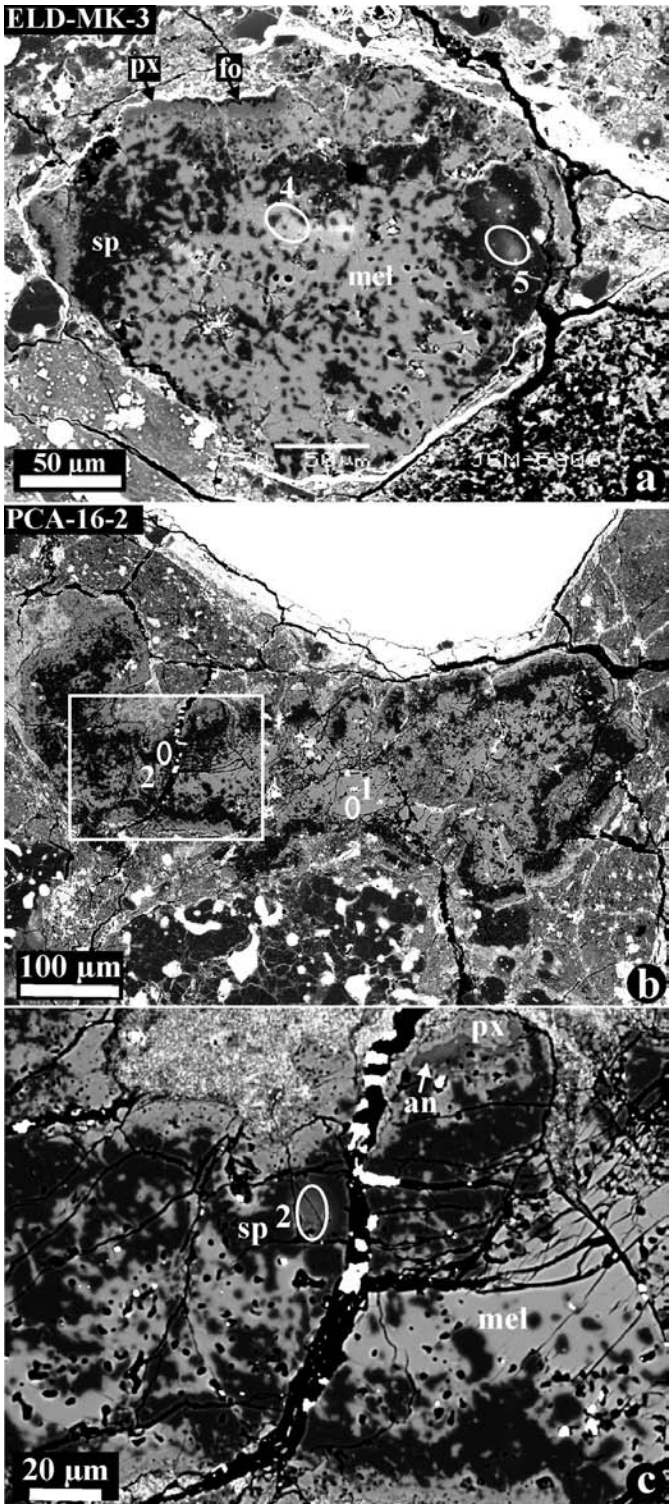

FIG. 3. BSE images of the melilite-rich CAIs ELD-MK-3 (a) and PCA-16-2 (b, c). Region outlined in (b) is shown in detail in (c). Both CAIs contain abundant anhedral grains of spinel and minor perovskite; minor anorthite occurs in PCA-16-2 (c). ELD-MK-3 (a) is surrounded by layers of pyroxene and forsterite (fo). PCA-16-2 (b, c) is surrounded by pyroxene rims only.

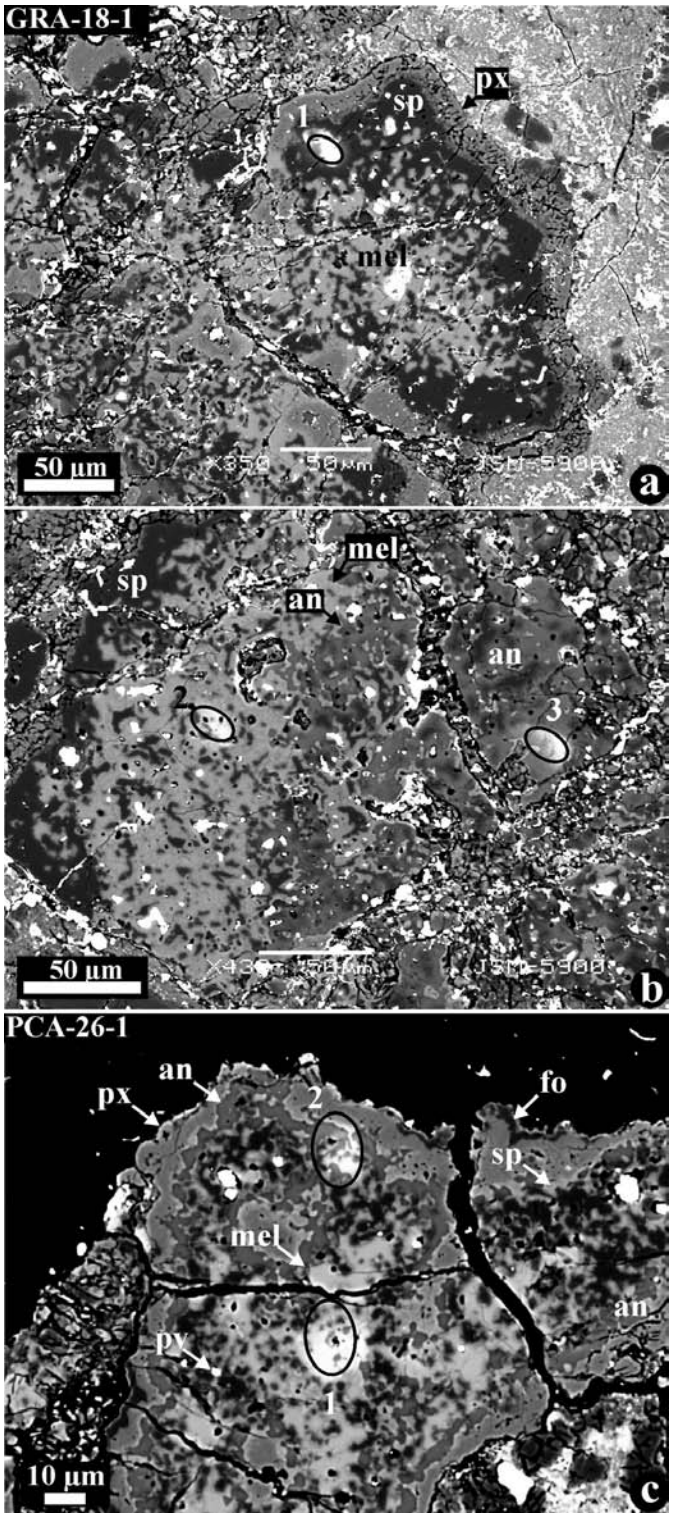

FIG. 4. BSE images of the melilite-anorthite-rich CAIs GRA-18-1 (a, b) and PCA-16-1 (c). Both CAIs contain abundant anhedral grains of spinel and anorthite and minor perovskite; anorthite replaces melilite. Bright grains in (a) and (c) represent Au coating used during Al-Mg-isotopic measurements. GRA-18-1 (a, b) is surrounded by a pyroxene rim; PCA-16-1 (c) is rimmed by pyroxene and forsterite layers.

(Fig. 6b). Other analyses show low totals and large enrichment in Al, Ca, and Si (SiO_2, 5.6; TiO_2, 0.08; Al_2O_3, 54.6; MnO, 0.29; CaO, 15.3; Na_2O, 0.42; total, 76.4 and SiO_2, 21.8; TiO_2, 0.15; Al_2O_3, 40.4; MgO, 0.42; CaO, 16.1; Na2O, 3.1; total, 82.2) and may represent hydrated grossite and melilite. The observed enrichment of the secondary regions in Na, Cl, and Si implies the presence of nepheline, sodalite, phyllosilicates or salts (Fig. 6e–j). The CAI fragment GRA-17-7 is surrounded by layers of spinel + hibonite and melilite (Fig. 6b), whereas the less fragmented GRA-17-8 is rimmed by layers of spinel + hibonite, melilite, anorthite, and pyroxene, with anorthite replacing melilite (Fig. 6d).

Spinel-Melilite-Pyroxene Calcium-Aluminum-Rich Inclusions–These CAIs (PCA-16-3, ELD-MK-2 and GRA-31-6) consist of aggregates of multiple fine-grained spinel-perovskite ± hibonite cores surrounded by melilite ± pyroxene rims (Fig. 7).

Pyroxene-Anorthite-Rich Calcium-Aluminum-Rich Inclusions–There are two textural varieties of the pyroxene-anorthite-rich CAIs. Most CAIs consist of irregularly-shaped pyroxene and anorthite grains with minor spinel and melilite; anorthite replaces melilite. The pyroxene-anorthite-rich CAI EET-21-3 contains two forsterite-rich fragments, both of which contain abundant FeNi-metal nodules and may represent chondrule fragments (Fig. 8). Although BSE images do not provide conclusive evidence as to whether these fragments are parts of the CAIs or were injected into the CAI during regolith gardening on the CR parent asteroid, x-ray elemental mapping showed the presence of a thin layer of FeO-rich material between the CAI and forsterite fragments which we attribute to matrix. Three of the pyroxene-anorthite-rich CAI fragments (ELD-154-10, MET-6-1 and MET-6-2) have igneous textures. The CAI fragment MET-6-1 consists of spinel-free anorthite-rich and spinel-rich pyroxene-melilite-anorthite portions (Fig. 9a,b). Spinel occurs as euhedral grains poikilitically enclosed by pyroxene, melilite, and anorthite. Melilite is an accessory phase that occupies interstitial regions between the anorthite laths. The CAI fragment MET-6-2 consists of Al-diopside, lath-shaped anorthite and euhedral spinel grains; melilite is very minor (Fig. 9c). The CAI fragment ELD-154-10 consists of lath-shaped anorthite and interstitial melilite and Al, Ti-diopside; all minerals poikilitically enclose euhedral spinel grains. Another pyroxene-anorthite-rich CAI fragment, GRA-18-22, consists of massive anorthite and anhedral grains of Al, Ti-diopside, both enclosing euhedral spinel grains (Fig. 10c). These CAIs have textural and mineralogical similarities with type B inclusions, but they have low melilite content and pyroxene is Al-diopside instead of fassaite.

Amoeboid Olivine Aggregates–The AOAs are aggregates of anhedral forsterite grains and refractory inclusions composed of spinel, pyroxene and anorthite; some of the AOAs contain rounded nodules of FeNi-metal (Fig. 11). In some cases, anhedral Al-diopside overgrows forsterite grains. Spinel grains are typically surrounded by anorthite and appear to be corroded by the latter.

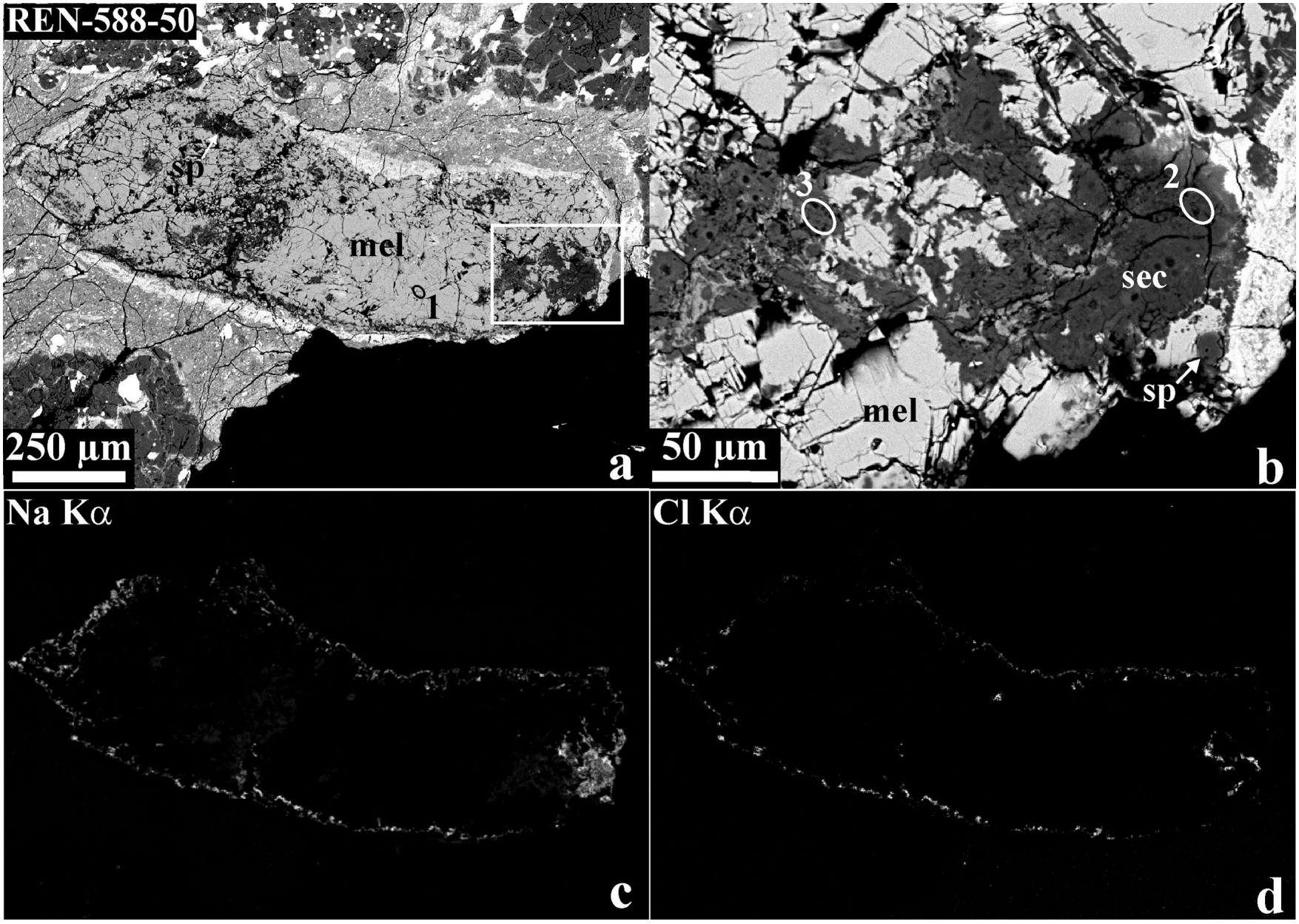

FIG. 5. BSE images (a, b) and x-ray elemental maps in Na (c) and Cl Kα (d) of the melilite-rich CAI REN-588-50 from Renazzo. The CAI consists of melilite and spinel; melilite is replaced by Cl-free (nepheline ?) and Cl-bearing (sodalite ?) secondary minerals (sec).

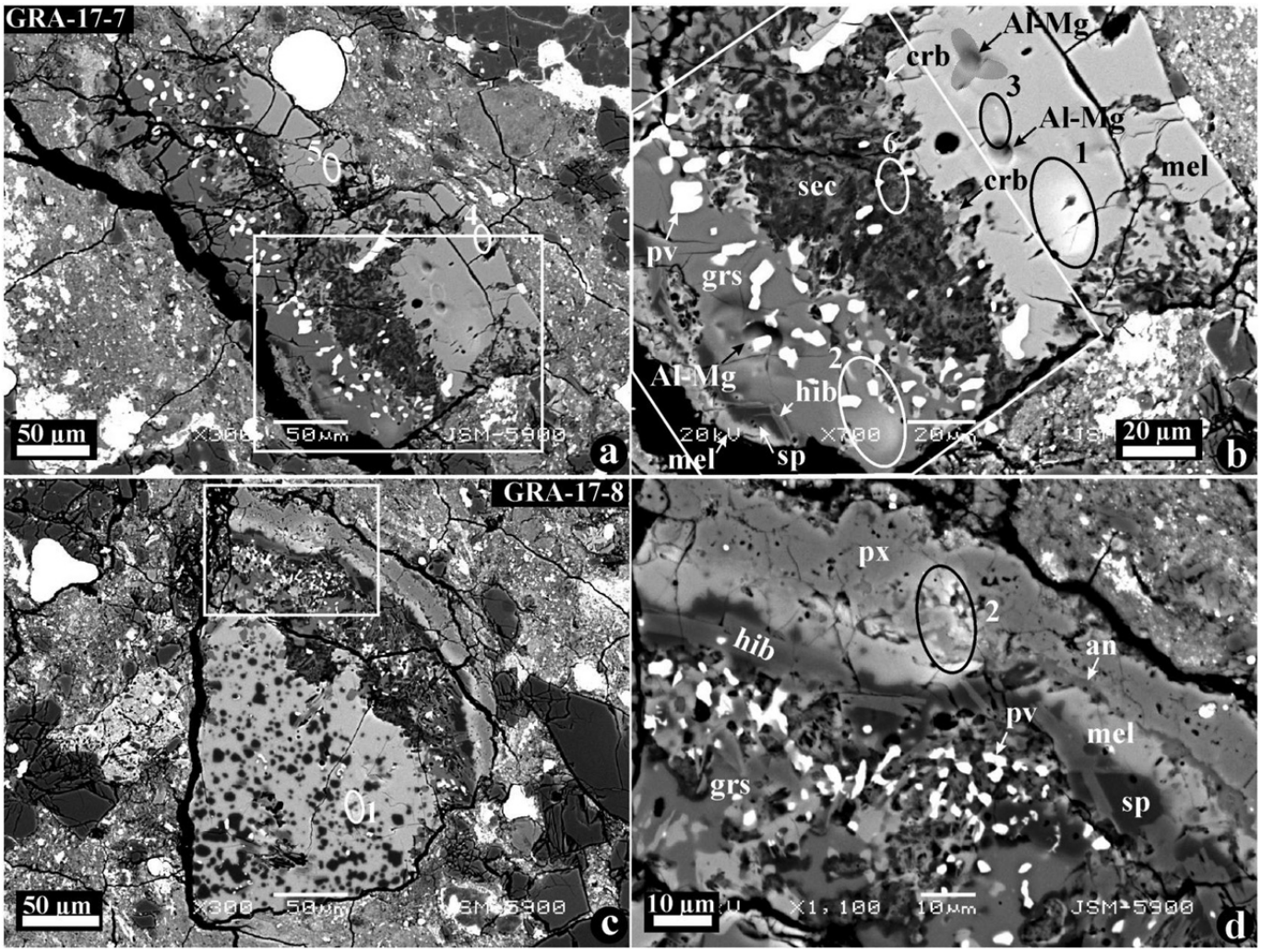

FIG. 6. BSE images (a–d) of the melilite-rich CAI fragments #GRA-17-7 (a, b) and GRA-17-8 (c, d). Regions outlined in (a) and (c) are shown in detail in (b) and (d), respectively. CAI GRA-17-7 (a, b) consists of a melilite core surrounded by a mantle composed of grossite, melilite, and perovksite. Hibonite, spinel and melilite (bottom left in (b)) probably represent part of a Wark–Lovering rim sequence. The region between the melilite core and the grossite mantle is heavily replaced by fine-grained secondary (sec) minerals, including Ca-rich carbonates (crb) and Na, Cl-bearing phases. Ion microprobe spots resulted from Al-Mg-isotopic measurements are labeled as "Al-Mg"; the shaded area outlines the region of shallow implantation of O atoms (see text). Core of the CAI GRA-17-8 (c, d) consists of melilite containing numerous inclusions of spinel and minor hibonite. It is surrounded by a mantle composed of grossite, hibonite, melilite, and perovksite and Wark–Lovering rim layers composed of spinel, hibonite, melilite, anorthite (an) and pyroxene. The outer portion of the melilite core contains rounded inclusions of grossite. The mantle is extensively replaced by fine-grained Na, Cl-bearing secondary minerals.

Mineral Chemistry

Representative microprobe analyses of hibonite, grossite, perovskite, melilite, and pyroxene are listed in Tables 2–4. Hibonite is MgO-poor (0.6–2.6 wt%) and TiO_2-rich (2.3–4.4 wt%) (Table 2). Grossite is nearly pure $CaAl_4O_7$ (Table 2). Perovskite is nearly pure $CaTiO_3$; the high concentration of Al_2O_3 in perovskite of the CAI GRA-17-7 is probably due to electron beam overlap onto the surrounding grossite (Table 2). Most melilite grains are Na-free and Mg-poor ($Åk_{5-40}$) (Table 3; Fig. 12). Melilite grains in individual CAIs typically have narrow compositional ranges (<15 mol% Åk). Spinel is FeO- and Cr_2O_3-poor (Fe/(Fe + Mg) ratio is generally <0.01; Cr_2O_3 < 0.5 wt%). There are no compositional differences between spinel grains in CAIs and AOAs. Pyroxene grains show large variations in Al_2O_3 (0.7–18 wt%) and TiO_2 (0.1–9.5 wt%) contents; these elements are positively correlated. Pyroxenes in Wark–Lovering rims and in AOAs have lower concentrations of Al_2O_3 and TiO_2 than those in CAI cores (Table 4). Most pyroxenes are Cr_2O_3-poor (<0.2 wt%) and MnO-free (<0.08 wt%). Olivine grains in AOAs are magnesium-rich ($Fa_{<3.5}$) (Fig. 13). The majority of the olivine grains have low contents of MnO (<0.4 wt%) and Cr_2O_3 (<0.4 wt%) (Fig. 14). Plagioclase is nearly end-member

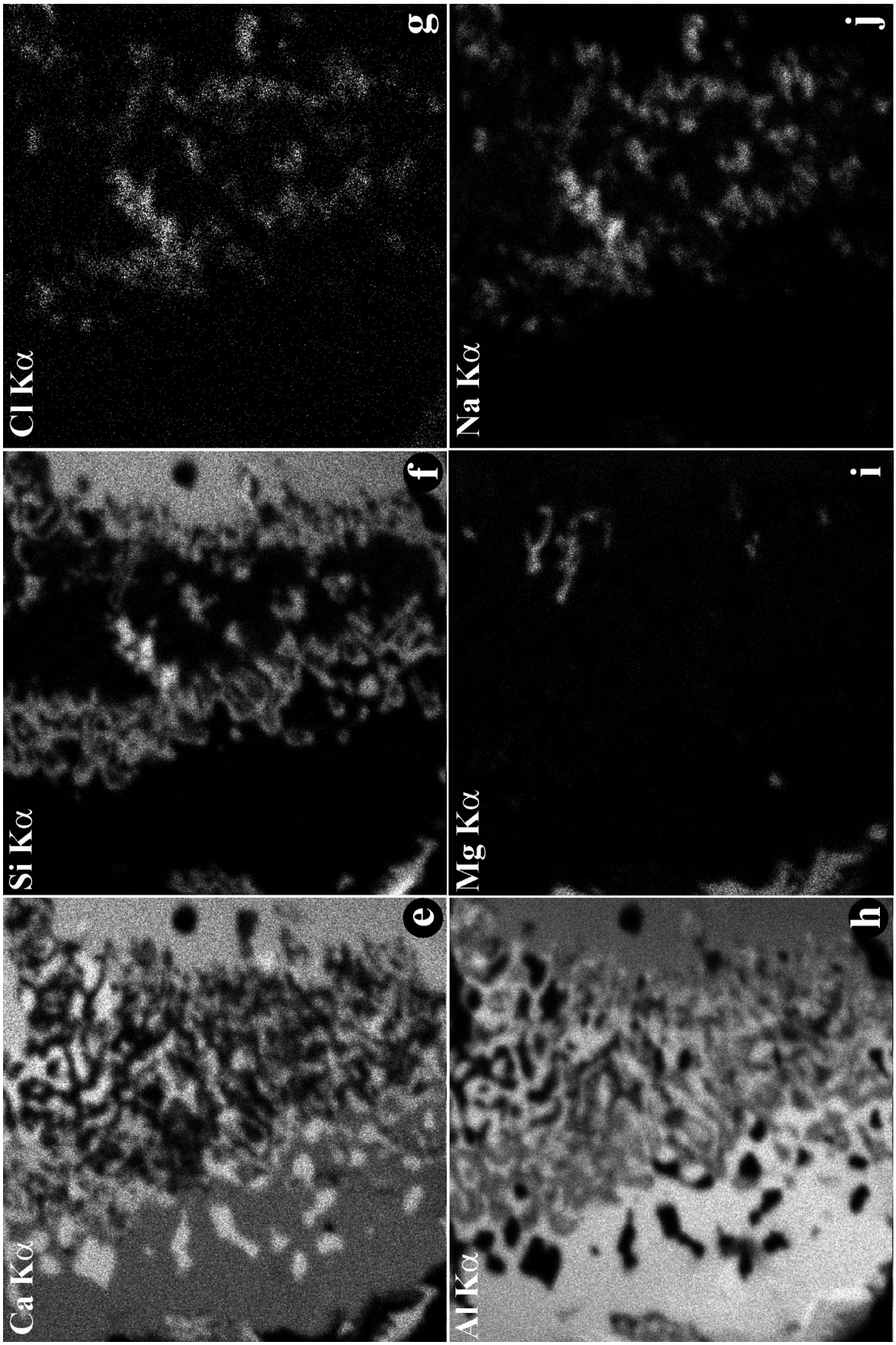

FIG. 6. (*Continued*) X-ray elemental maps in Ca (e), Si (f), Cl (g), Al (h), Mg (i) and Na Kα (j) of the melilite-rich CAI fragments #GRA-17-7 (e–j). Region outlined in (b) is shown in (e–j).

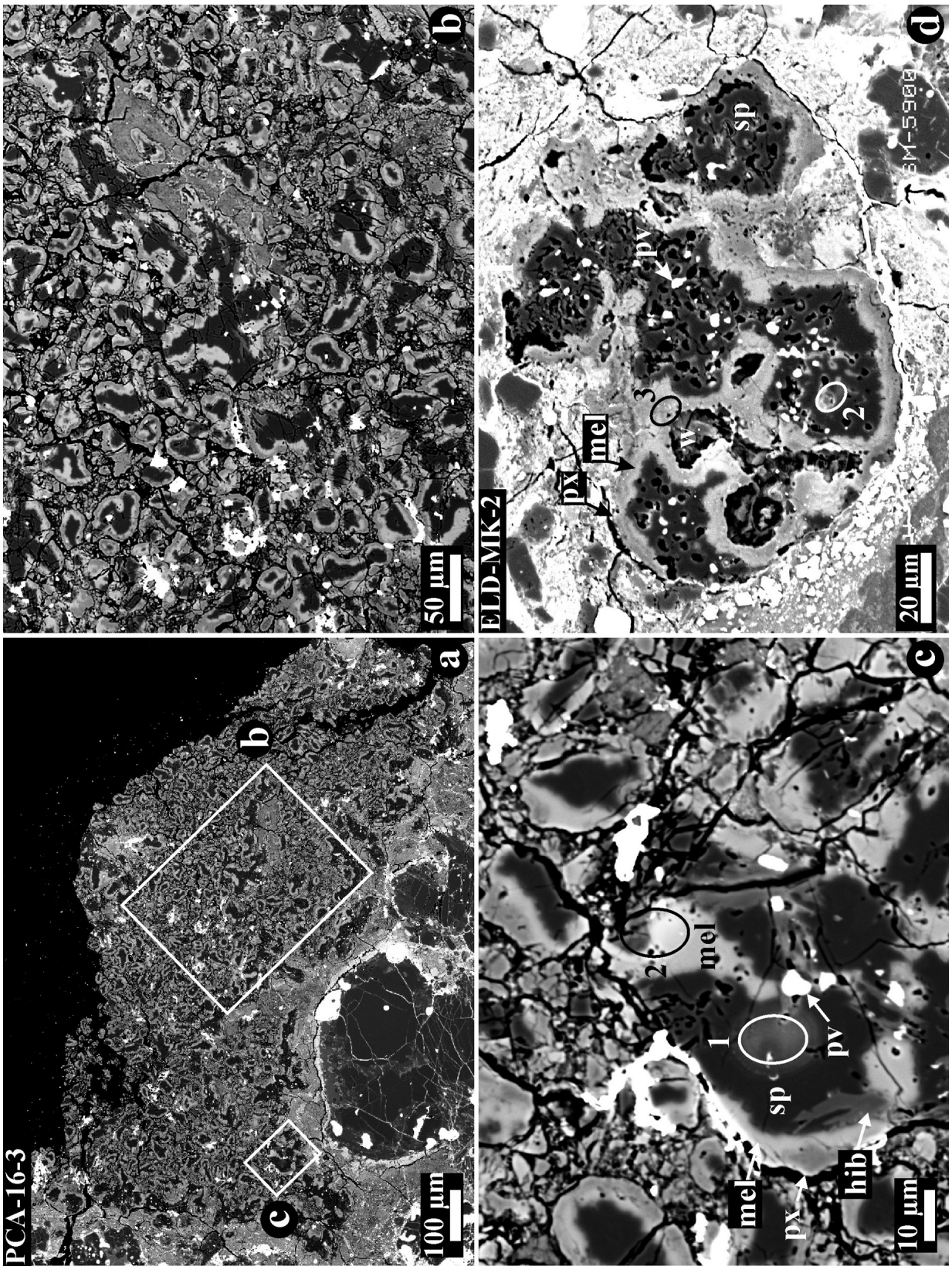

FIG. 7. BSE images of the fine-grained spinel-rich CAIs PCA-16-3 (a–c) and ELD-MK-2 (d). Each core consists of spinel, perovskite (and hibonite in PCA-16-3) and is surrounded by melilite and pyroxene layers.

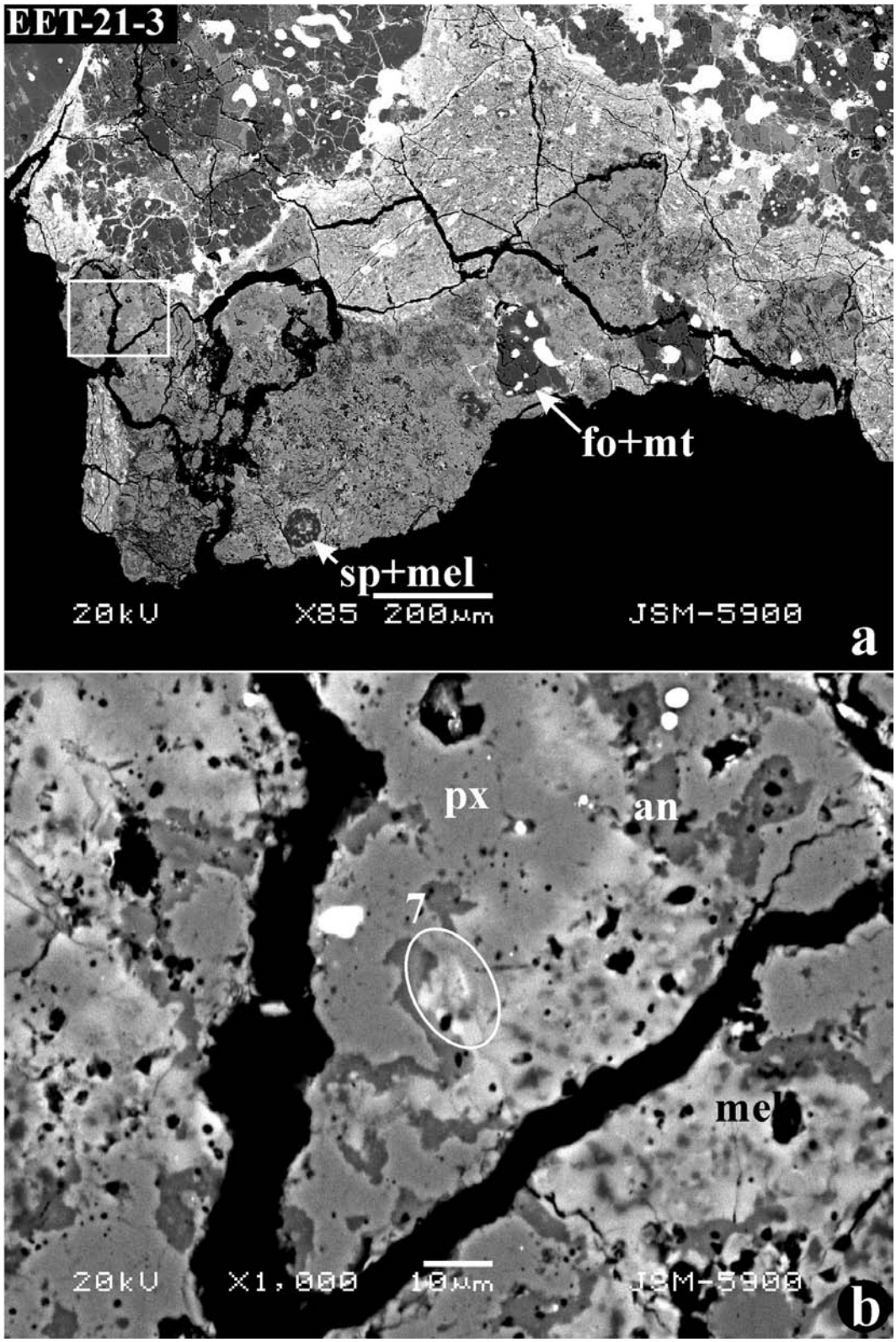

FIG. 8. BSE images of a pyroxene-anorthite-rich CAI EET-21-3. The CAI consists of pyroxene, anorthite, spinel and melilite. Regions outlined in (a) is shown in detail in (b). Two forsterite fragments containing FeNi-metal nodules probably represent chondrule fragments.

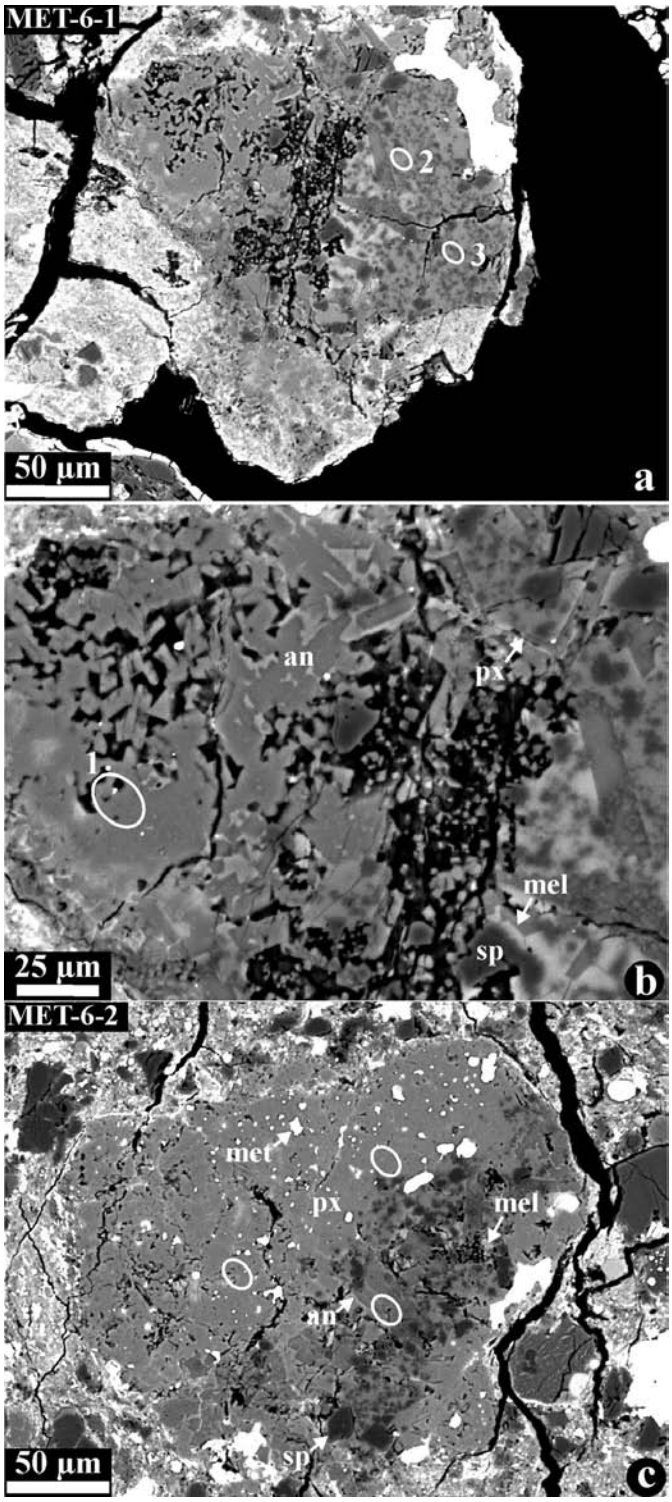

FIG. 9. BSE images of the CAI fragments MET-6-1 (a, b) and MET-6-2 (c). Both fragments consist of Al-diopside, lath-shaped anorthite, and melilite; all the phases poikilitically enclose euhedral spinel grains. CAI MET-6-2 (c) contains rounded FeNi-metal nodules.

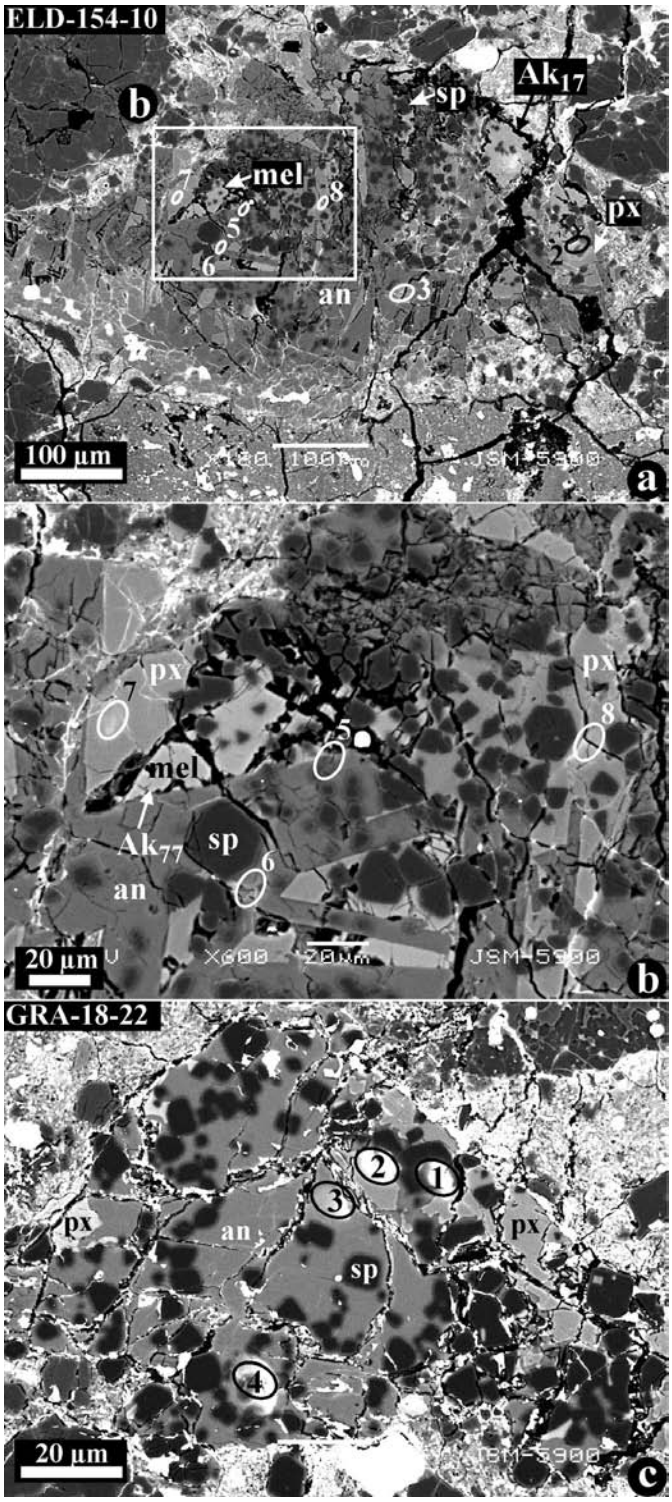

FIG. 10. BSE images of the CAIs ELD-154-10 (a, b) and GRA-18-22 (c). Region outlined in (a) is shown in detail in (b). ELD-154-10 consists of lath-shaped anorthite and interstitial melilite ($Åk_{77}$) and pyroxene. All minerals poikilitically enclose euhedral spinel grains. One of the melilite grains is Åk-poor ($Åk_{16}$) and could be relic. GRA-18-22 consists of anorthite and anhedral grains of Al, Ti-diopside; both poikilitically enclose euhedral grains of spinel.

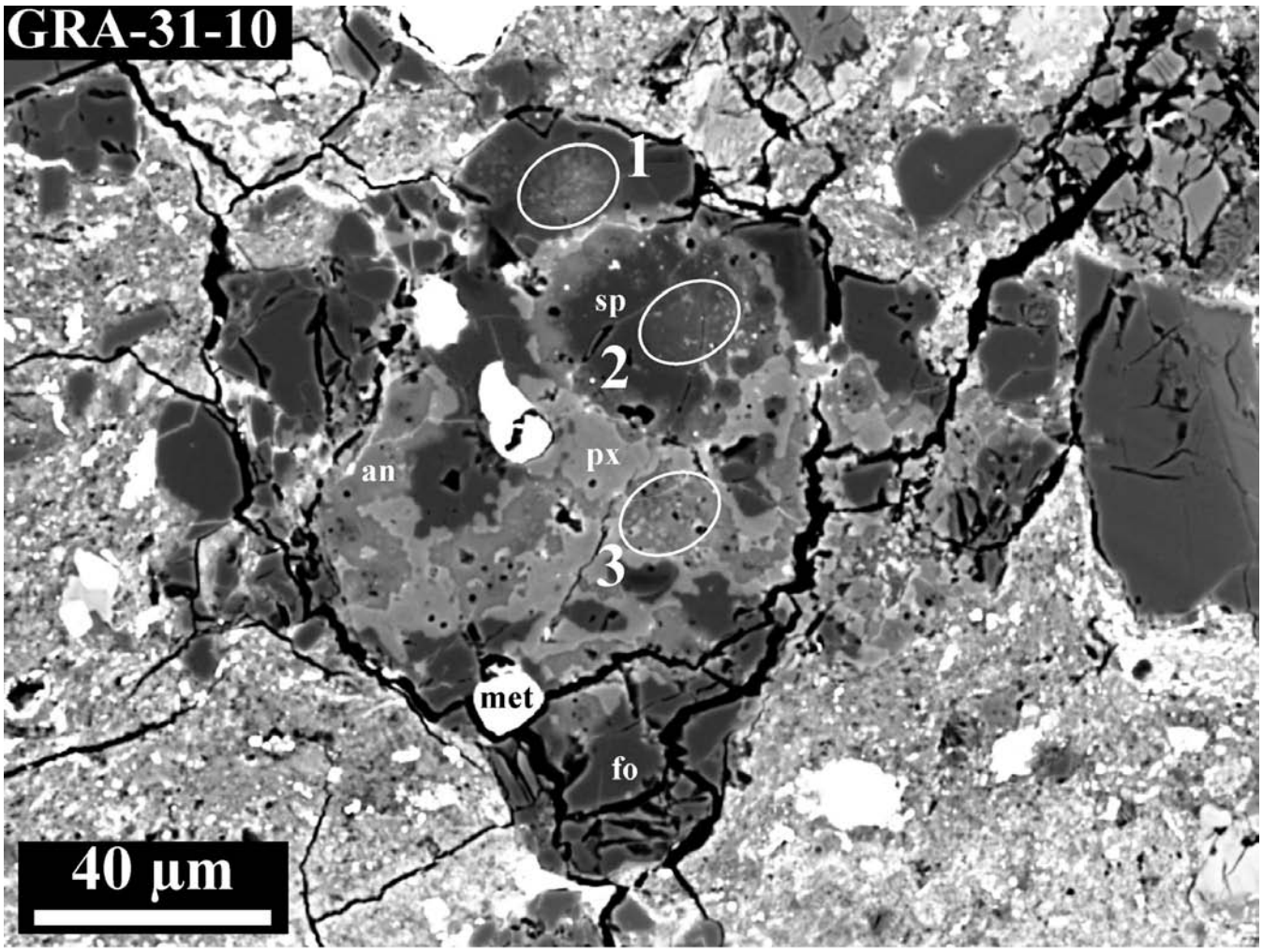

FIG. 11. BSE image of an AOA GRA-31-10. It consists of forsterite, spinel, pyroxene, anorthite and minor FeNi-metal. The anhedral spinel grains are surrounded by anorthite; pyroxene overgrows forsterite.

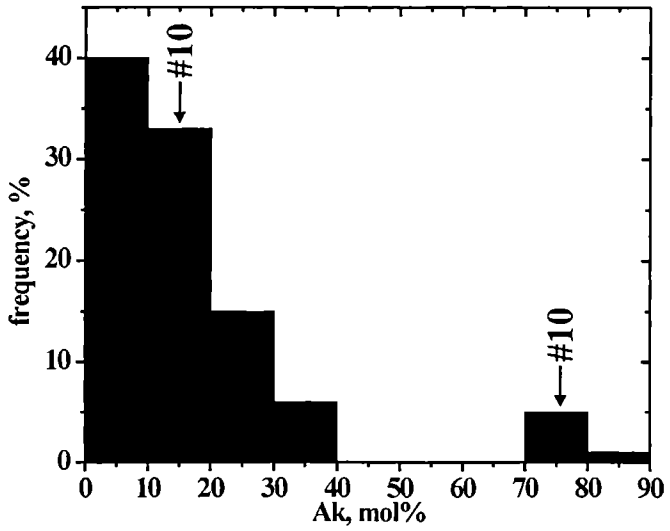

FIG. 12. Histogram of Åk contents (in mol%) in melilite in CAIs in CR chondrites.

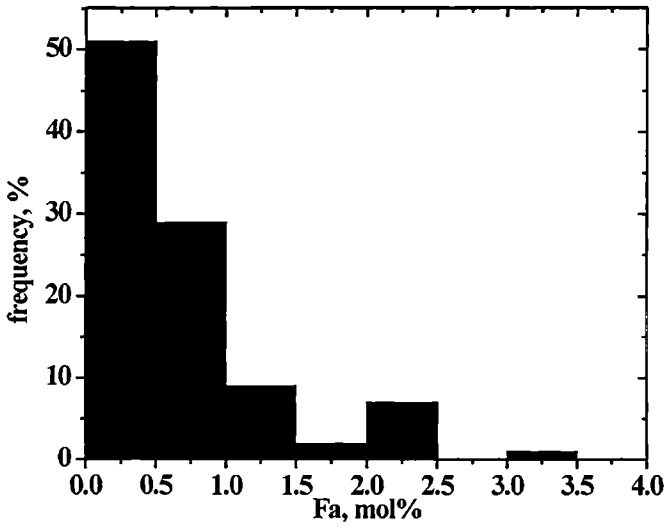

FIG. 13. Histogram of Fa contents (in mol%) in forsterite in CAIs in CR chondrites.

TABLE 2. Representative microprobe analyses of hibonite, grossite and perovskite in CAIs in CR chondrites.

Analysis	1	2	3	4	5	6	7	8
Mineral/oxide	hib	hib	hib	grs	grs	grs	grs	pv
SiO_2	0.27	0.05	0.39	0.03	0.07	0.23	<0.04	0.12
TiO_2	2.7	2.3	4.4	0.21	0.10	0.02	0.14	57.8
Al_2O_3	87.5	89.6	84.4	78.5	78.3	77.0	78.5	0.87
Cr_2O_3	<0.07	<0.07	0.08	<0.07	<0.07	<0.07	<0.07	<0.07
FeO	0.46	0.41	<0.09	0.14	0.42	<0.09	0.33	0.18
MnO	<0.08	<0.08	<0.08	<0.08	<0.08	<0.08	<0.08	<0.08
MgO	1.5	0.62	2.6	<0.06	<0.06	0.09	<0.06	<0.06
CaO	8.4	8.4	8.4	21.6	21.4	22.3	21.4	40.3
Na_2O	<0.08	<0.08	<0.08	<0.08	<0.08	<0.08	<0.08	<0.08
K_2O	<0.04	<0.04	<0.04	<0.04	<0.04	<0.04	<0.04	<0.04
Total	100.8	101.3	100.3	100.5	100.3	99.7	100.4	99.3
	Structural formulae based on:							
	19 O	19 O	19 O	7 O	7 O	7 O	7 O	3 O
Si	0.030	0.006	0.044	0.001	0.003	0.010	0.001	0.003
Ti	0.227	0.193	0.373	0.007	0.003	0.001	0.005	0.986
Al	11.461	11.646	11.143	3.986	3.987	3.952	3.990	0.023
Cr	–	–	0.007	–	–	–	–	–
Fe	0.042	0.038	0.008	0.005	0.015	0.000	0.012	0.003
Mn	–	–	–	–	–	–	–	–
Mg	0.243	0.102	0.427	–	–	–	–	–
Ca	1.005	0.989	1.007	0.999	0.989	1.041	0.990	0.981
Na	–	–	–	–	–	–	–	–
K	–	–	–	–	–	–	–	–
Total	13.011	12.978	13.009	4.999	5.001	5.012	5.000	1.998

1 = GRA-30-7; 2 = ELD-MK-5; 3 and 4 = GRA-17-8; 5 and 8 = GRA-17-7; 6 = ELD-MK–5; 7 = GRA-31-3; hib = hibonite; grs = grossite; pv = perovskite; GRA = Graves Nunataks; ELD = El Djouf.

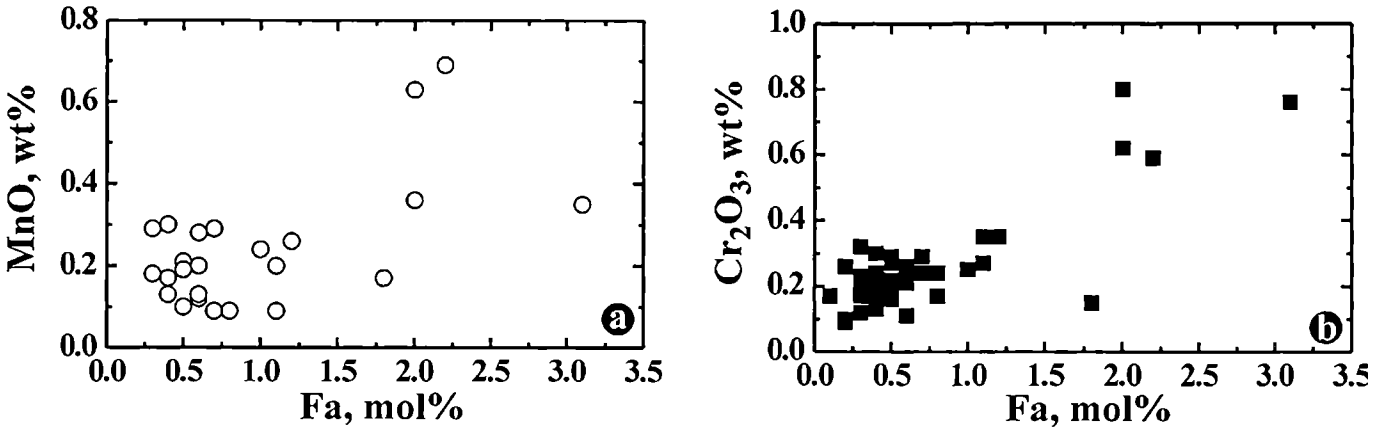

FIG. 14. Concentrations (in wt%) of MnO and Cr_2O_3 *vs.* Fa content in forsterite in AOAs in CR chondrites.

TABLE 3. Representative microprobe analyses of melilite in CAIs in CR chondrites.

Analysis	1	2	3	4	5*	6	7	8	9	10*	11	12	13	14	15	16	17	18	19
SiO_2	24.3	28.2	22.5	24.4	23.8	25.4	30.0	23.3	22.8	25.0	24.1	27.5	22.6	23.8	23.7	27.2	25.6	39.0	40.5
TiO_2	0.08	<0.05	0.15	0.08	<0.05	<0.05	0.05	<0.05	0.08	<0.05	0.08	<0.05	0.06	<0.05	0.11	<0.05	<0.05	0.10	<0.05
Al_2O_3	32.8	26.5	36.6	33.0	34.4	31.8	24.8	34.2	36.2	31.5	33.5	28.0	35.2	33.2	33.9	28.7	30.4	9.0	6.5
Cr_2O_3	<0.07	<0.07	<0.07	<0.07	<0.07	<0.07	<0.07	<0.07	<0.07	<0.07	<0.07	<0.07	<0.07	<0.07	<0.07	<0.07	<0.07	<0.07	<0.07
FeO	0.22	0.29	<0.09	<0.09	0.11	<0.09	<0.09	0.18	0.18	0.25	<0.09	<0.09	<0.09	<0.09	<0.09	<0.09	0.36	0.31	0.37
MnO	<0.08	<0.08	<0.08	<0.08	<0.08	<0.08	<0.08	<0.08	<0.08	<0.08	<0.08	<0.08	<0.08	<0.08	0.09	<0.08	<0.08	<0.08	<0.08
MgO	2.6	3.9	0.74	1.6	1.0	2.1	4.9	0.92	2.1	2.1	2.2	3.6	0.9	1.6	2.5	3.4	2.6	10.6	12.1
CaO	40.3	40.8	40.4	40.9	40.7	40.4	41.0	40.5	38.1	40.2	39.9	40.7	40.6	40.6	39.1	39.5	41.7	40.9	40.4
Na_2O	<0.08	<0.08	<0.08	<0.08	<0.08	<0.08	<0.08	<0.08	<0.08	<0.08	<0.08	<0.08	<0.08	<0.08	<0.08	0.10	<0.08	0.25	0.12
K_2O	<0.04	<0.04	<0.04	<0.04	<0.04	<0.04	<0.04	<0.04	<0.04	<0.04	<0.04	<0.04	<0.04	<0.04	<0.04	<0.04	<0.04	<0.04	<0.04
Total	100.5	99.7	100.6	100.1	100.1	99.9	100.9	99.2	99.6	99.1	99.9	100.0	99.4	99.2	99.4	98.8	100.7	100.2	100.2
								Structural formulae based on 7 O:											
Si	1.105	1.290	1.020	1.112	1.086	1.157	1.353	1.073	1.038	1.150	1.096	1.253	1.037	1.095	1.081	1.247	1.166	1.771	1.836
Ti	0.003	–	0.005	0.003	–	–	0.002	–	0.003	–	0.003	–	0.002	–	0.004	–	–	0.004	–
Al	1.756	1.429	1.956	1.773	1.847	1.709	1.317	1.857	1.940	1.707	1.799	1.503	1.907	1.800	1.826	1.551	1.630	0.481	0.349
Cr	–	–	–	–	–	–	–	–	–	–	–	–	–	–	–	–	–	–	–
Fe	0.008	0.011	–	–	0.004	–	–	0.007	0.007	0.009	–	–	–	–	–	–	0.014	0.012	0.014
Mn	–	–	–	–	–	–	–	–	–	–	–	–	–	–	–	–	–	–	–
Mg	0.177	0.269	0.050	0.112	0.068	0.142	0.330	0.063	0.143	0.142	0.148	0.246	0.060	0.109	0.172	0.231	0.176	0.715	0.815
Ca	1.963	1.997	1.961	1.996	1.985	1.970	1.982	1.997	1.856	1.983	1.950	1.988	1.998	1.998	1.914	1.942	2.029	1.989	1.962
Na	–	–	–	–	–	–	–	–	–	–	–	–	–	–	–	–	–	0.022	0.010
K	–	–	–	–	–	–	–	–	–	–	–	–	–	–	–	–	–	–	–
Total	5.017	4.996	4.996	4.998	4.992	4.978	4.983	5.000	4.989	4.994	5.002	4.996	5.007	5.005	5.002	4.982	5.018	4.996	4.986
Ak	10.5	29.0	2.0	11.2	8.6	15.7	35.3	7.3	3.8	15.0	9.6	25.3	3.7	9.5	8.1	24.7	16.6	77.1	83.7

1 and 2 = GRA-31-3; 3 to 5 = GRA-17-8; 6 and 7 = REN-588-50; 8 = EET-21-12; 9 and 10 = ELD-MK-3; 11 and 12 = GRA-18-1; 13 and 14 = GRA-31=2; 15 and 16 = EET-21-3; 17 and 18 = ELD-154-10; 19 = MET-6-1.

*Rim melilite.

Abbreviations: GRA = Graves Nunataks; REN = Renazzo; EET = Elephant Moraine; ELD = El Djouf; MET = Meteorite Hills.

TABLE 4. Representative microprobe analyses of pyroxenes in CAIs and AOAs in CR chondrites.

Oxide\ analysis	1	2	3*	4*	5	6	7	8	9	10	11	12	13	14	15	16	17
SiO_2	42.0	35.3	54.4	49.0	54.1	52.5	45.8	42.0	38.8	45.5	50.2	45.2	55.2	51.8	48.4	47.0	44.0
TiO_2	2.6	9.1	0.64	0.63	0.09	0.30	3.5	5.3	6.4	1.4	0.94	0.45	0.06	0.55	2.9	2.2	3.6
Al_2O_3	13.4	18.5	2.2	9.7	2.3	4.6	11.9	15.3	19.5	16.0	8.7	18.3	1.3	6.5	6.4	9.7	13.2
Cr_2O_3	0.09	0.08	<0.07	0.10	0.11	0.17	0.10	1.1	0.28	0.25	0.52	0.23	<0.07	<0.07	0.09	<0.07	0.36
FeO	5.6	3.3	0.38	0.63	<0.09	<0.09	<0.09	0.47	0.72	0.86	0.56	0.68	0.53	0.28	0.97	0.60	0.28
MnO	<0.08	<0.08	<0.08	<0.08	<0.08	<0.08	<0.08	<0.08	<0.08	<0.08	0.12	0.21	<0.08	<0.08	<0.08	<0.08	<0.08
MgO	11.4	8.0	19.1	16.0	17.5	16.6	13.1	11.2	9.9	12.1	15.1	11.3	19.9	16.0	15.7	14.5	13.4
CaO	23.1	23.6	24.5	24.7	25.7	25.6	25.4	25.4	25.3	24.9	24.9	25.0	23.7	25.5	24.2	25.0	24.5
Na_2O	<0.08	<0.08	<0.08	<0.08	<0.08	<0.08	<0.08	<0.08	<0.08	<0.08	<0.08	<0.08	<0.08	<0.08	<0.08	<0.08	<0.08
K_2O	<0.04	<0.04	<0.04	<0.04	<0.04	<0.04	<0.04	<0.04	<0.04	<0.04	<0.04	<0.04	<0.04	<0.04	<0.04	<0.04	<0.04
Total	98.2	97.9	101.2	100.7	99.8	99.8	99.8	100.8	100.7	100.9	101.1	101.4	100.8	100.7	98.7	99.1	99.3
								Structural formulae based on 6 O:									
Si	1.595	1.350	1.933	1.758	1.953	1.897	1.669	1.531	1.416	1.634	1.797	1.614	1.966	1.857	1.783	1.725	1.613
Ti	0.073	0.260	0.017	0.017	0.002	0.008	0.096	0.144	0.175	0.037	0.025	0.012	0.002	0.015	0.081	0.062	0.099
Al	0.601	0.833	0.092	0.411	0.096	0.197	0.509	0.658	0.838	0.678	0.369	0.768	0.056	0.274	0.278	0.418	0.572
Cr	0.003	0.002	–	0.003	0.003	0.005	0.003	0.030	0.008	0.007	0.015	0.007	–	–	0.003	–	0.011
Fe	0.177	0.105	0.011	0.019	0.001	0.003	0.000	0.014	0.022	0.026	0.017	0.020	0.016	0.008	0.030	0.018	0.009
Mn	–	–	–	–	–	–	–	–	–	–	0.004	0.006	–	–	–	–	–
Mg	0.644	0.456	1.015	0.855	0.943	0.893	0.714	0.610	0.540	0.647	0.806	0.601	1.058	0.855	0.864	0.795	0.730
Ca	0.938	0.964	0.932	0.952	0.994	0.991	0.989	0.992	0.988	0.957	0.954	0.957	0.904	0.978	0.955	0.982	0.962
Na	–	–	–	–	–	–	–	–	–	–	–	–	–	–	–	–	–
K	–	–	–	–	–	–	–	–	–	–	–	–	–	–	–	–	–
Total	4.029	3.971	4.000	4.016	3.993	3.993	3.979	3.979	3.986	3.985	3.986	3.986	4.003	3.988	3.994	4.000	3.994

1 to 12 = CAIs; 13 to 17 = AOAs; 1 and 2 = GRA-18-22; 3 and 4 = GRA-31-3; 5 to 7 = EET-21-3; 8 and 9 = ELD-154-10; 10 = MET-6-1; 11 and 12 = MET-6-2; 13 = ELD-154-52; 14 = ELD-154-60; 15 and 16 = GRA-31-10; 17 = PCA-26-2.

*Rim pyroxenes.

Abbreviations: GRA = Graves Nunataks; EET = Elephant Moraine; ELD = El Djouf; MET = Meteorite Hills; PCA = Pecora Escarpment.

anorthite ($CaAl_2Si_2O_8$); concentrations of Na_2O are below the detection limit of electron microprobe analysis (<0.08 wt%). Minerals in the igneous pyroxene-anorthite-rich CAIs have some unusual compositional signatures. Spinel grains are enriched in Cr_2O_3 (~1 wt%). Melilite is more Åk-rich than in other CAI types from CR chondrites (Table 3). In ELD-154-10, melilite shows large compositional variations in Åk contents (17–77 mol%) and contains detectable concentrations of Na_2O (0.25 wt%). Most melilite grains in this CAI occupying interstitial regions between anorthite laths are compositionally uniform and Åk-rich (~77 mol%); the lowest Åk-content is found in a single melilite grain, which could be a relic grain (Fig. 10a). The highest Åk-content (83.7 mol%) was found in melilite of another igneous pyroxene-anorthite-rich CAI, MET-6-1 (Table 3). Pyroxenes contain about 0.3–1 wt% of Cr_2O_3 and have low concentrations of TiO_2 (0.5–6 wt%) relative to pyroxenes in type B CAIs from CV chondrites (Table 4; MacPherson *et al.*, 1988).

Oxygen-Isotopic Composition

Most primary minerals in the CR CAIs and AOAs have ^{16}O-rich compositions ($-50‰ < \delta^{17}O, \delta^{18}O < -25‰$ or $-25‰ < \Delta^{17}O < -13‰$) and plot along the CCAM line (Table 5; Fig. 15). Although there is a significant spread along this line, the primary minerals within individual CAIs are largely homogeneous in oxygen-isotopic composition. There are several important exceptions to the generally ^{16}O-rich nature of CR CAIs and AOAs:

(1) Five clearly igneous CAIs (pyroxene-anorthite-rich CAIs: ELD-154-10, GRA-18-22, MET-6-1 and -2, and melilite-rich CAI, GRA-18-3) have relatively ^{16}O-poor compositions ($\Delta^{17}O = -3‰$ to $-18‰$). A spread between $\Delta^{17}O = -6.1 \pm 1.7‰$ and $\Delta^{17}O = -18.1 \pm 2.1‰$ is observed in ELD-154-10, whereas the other igneous CAIs are isotopically homogeneous (Table 5; Fig. 16).

(2) The forsterite-metal fragments in EET-21-3 fall on the CCAM line and have ^{16}O-excesses ($\Delta^{17}O \approx -5.7 \pm 1.9‰$) similar to forsterite in CR chondrules (Leshin *et al.*, 2000).

(3) Oxygen-isotopic compositions of the grossite-hibonite CAI ELD-MK-5 spread between $\Delta^{17}O = -13.3 \pm 2.2‰$ and $\Delta^{17}O = -23.3 \pm 1.3‰$, with grossite slightly depleted in ^{16}O relative to hibonite.

(4) The grossite-bearing melilite-rich CAI fragment GRA-17-8 has a relatively ^{16}O-poor melilite-anorthite-pyroxene rim ($\Delta^{17}O = -15.2 \pm 1.8‰$) compared to an ^{16}O-rich melilite core ($\Delta^{17}O = -24.7 \pm 1.7‰$).

(5) The secondary alteration minerals (phyllosilicates?) in GRA-17-7 plot at the intersection of the CR mixing line (Clayton and Mayeda, 1999) and the terrestrial fractionation (TF) line ($\delta^{18}O = 18.3 \pm 0.3‰$, $\delta^{17}O = -1.0 \pm 2.2‰$; Fig 15). In REN-588-50 the secondary Na-bearing alteration minerals plot at the intersection of the CCAM line and the TF line ($\delta^{18}O \approx +7‰$, $\delta^{17}O = 0.2 \pm 1.0‰$).

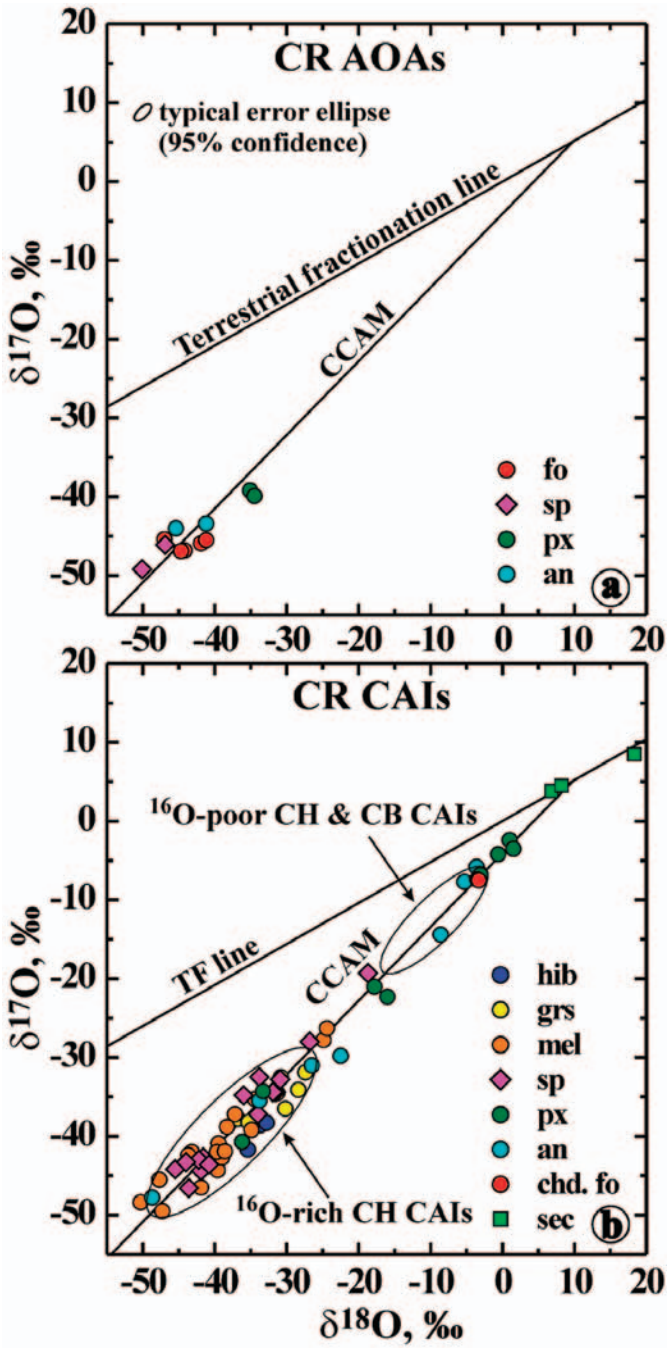

FIG. 15. Oxygen-isotopic composition of the CR AOAs (a) and CAIs (b). The forsterite-metal inclusions (fo-met) in the CAI EET-21-3 are probably chondrule fragments. Secondary minerals in the CAIs GRA-17-7 and REN-588-50 lie on the terrestrial mass fractionation line (TF line). The latter and the carbonaceous chondrites anhydrous minerals mixing line (CCAM line) are given for reference. Envelopes of data for CAIs from the CB and CH chondrites (Krot *et al.*, 2001a; Sahijpal *et al.*, 1999) are shown for comparison. The error ellipse is typical of the error ellipse of each spot with a 95% confidence interval (~2σ).

TABLE 5. Ion microprobe analyses of oxygen-isotopic compositions (‰) of CAIs and AOAs in CR chondrites.

Sample	Minerals analyzed	Spot	$\delta^{18}O$	2σ	$\delta^{17}O$	2σ	$\Delta^{17}O$	2σ*
ELD-MK-5	hib	10	−35.4	1.5	−41.7	1.6	−23.3	1.3
	hib + grs	4	−33.7	1.6	−38.6	2.6	−21.1	2.4
	hib	5	−32.8	1.7	−38.3	2.0	−21.2	1.8
	grs	9	−30.2	1.6	−36.5	1.7	−20.8	1.5
	grs (+pv)	8	−28.4	1.5	−34.1	1.7	−19.3	1.4
	grs (+pv)	7	−27.4	1.5	−31.9	1.8	−17.6	1.6
	grs (+pv + w)	6	−20.5	1.6	−24.0	2.4	−13.3	2.2
GRA-31-3	grs (+mel)	1	−30.8	1.6	−32.5	2.4	−16.5	2.2
	grs (+mel)	2	−36.8	1.7	−37.8	1.8	−18.7	1.5
GRA-17-7	grs (+pv)	2	−35.3	1.6	−38.2	1.9	−19.9	1.7
	mel	5	−39.6	1.6	−44.3	1.7	−23.7	1.5
	sec	6	18.3	1.5	8.5	1.5	−1.0	1.2
	mel	1†	−47.3	1.8	−49.5	2.2	−24.9	2.1
	mel	3†	−55.9	2.1	−59.0	2.3	−29.9	2.2
GRA-17-8	mel (+sp)	1	−41.9	1.7	−46.5	1.8	−24.7	1.7
	rim px + an + mel	2	−27.8	1.6	−29.7	2.0	−15.2	1.8
GRA-31-6	mel (+sp)	1	−34.4	1.7	−35.3	2.2	−17.4	2.1
PCA-16-3	sp	1	−45.5	1.6	−44.2	2.2	−20.6	2.0
	mel + px	2	−43.2	1.7	−42.0	3.0	−19.5	2.9
ELD-MK-2	sp (+mel)	2	−41.9	1.5	−44.4	1.6	−22.6	1.3
	px (+mel + w)	3	−36.2	1.6	−40.7	1.7	−21.9	1.5
GRA-18-1	sp	1	−26.8	1.7	−28.0	1.9	−14.0	1.8
	mel (+sp)	2	−24.9	1.6	−27.8	2.5	−14.8	2.3
	an (+px)	3	−26.5	1.6	−31.0	1.7	−17.2	1.5
GRA-31-8	mel	1	−38.6	1.6	−41.9	2.8	−21.8	2.6
PCA-16-1	mel (+sp)	1	−43.7	1.7	−42.4	1.8	−19.7	1.6
	an (+px + sp)	2	−48.7	1.6	−47.8	2.4	−22.5	2.2
PCA-16-2	mel	1	−38.3	1.6	−38.8	2.2	−18.9	2.0
	sp	2	−44.0	1.6	−43.3	2.4	−20.4	2.3
ELD-MK-3	mel (+sp)	4	−34.9	1.6	−39.2	2.1	−21.1	1.9
	sp	5	−42.2	1.6	−43.0	1.8	−21.1	1.6
EET-21-12	mel	1	−31.3	1.5	−34.5	2.0	−18.2	1.8
	sp (+mel)	2	−34	1.6	−37.2	2.2	−19.5	2.1
REN-588-50	mel	1	−39.0	1.5	−42.7	1.4	−22.4	1.0
	sec	2	6.8	1.5	3.8	1.3	0.2	0.9
	sec	3	8.2	1.5	4.5	1.5	0.2	1.2
EET-10-1	mel (+sp + pv)	1	−47.0	1.6	−45.4	1.8	−21.0	1.5
	mel (+sp + pv)	2	−50.1	1.6	−49.2	2.2	−23.2	2.0
GRA-31-2	mel	1	−39.5	1.6	−40.9	1.9	−20.4	1.7
	mel	3	−39.7	1.6	−42.0	2.2	−21.4	2.0
	sp	2	−41.6	1.6	−42.7	2.6	−21.1	2.4
GRA-18-3	mel (+sp)	1	−37.2	1.9	−37.2	1.8	−17.8	1.7
	sp (+mel)	2	−31.9	1.6	−34.4	2.3	−17.8	2.1
GRA-18-2	mel	1	−24.4	1.6	−26.3	1.7	−13.6	1.5
EET-21-3	sp	8	−43.6	1.6	−46.6	1.7	−23.9	1.4
	sp (+mel)	1	−40.8	1.6	−43.6	1.8	−22.4	1.6
	sp + px (+an)	2	−31.5	1.6	−34.4	2.2	−18.1	2.0
	px	6	−32.9	1.6	−40.0	1.8	−22.9	1.6
	px	9	−38.2	1.6	−43.6	2.0	−23.7	1.8
	px + mel (+an)	7	−37.2	1.6	−44.2	1.9	−24.8	1.7
	fo	3	−3.5	1.6	−7.4	2.1	−5.6	1.9
	fo	5	−3.3	1.6	−7.5	2.0	−5.8	1.8
MET-6-1	an	1	−5.3	1.5	−7.7	1.6	−5.0	1.4
	px + sp	2	−0.6	1.5	−4.2	1.3	−4.0	0.9
	px + sp	3	−3.1	1.5	−6.8	1.4	−5.2	1.0

TABLE 5. *Continued.*

Sample	Minerals analyzed	Spot	$\delta^{18}O$	2σ	$\delta^{17}O$	2σ	$\Delta^{17}O$	2σ*
MET–6–2	px	1	1.0	1.5	–2.4	1.3	–2.9	1.0
	an + px	2	–3.6	1.5	–5.8	1.4	–3.9	1.1
	px	4	1.5	1.5	–3.5	1.5	–4.3	1.2
GRA–18–22	sp (+px)	1	–33.8	1.6	–32.5	2.1	–14.9	1.9
	sp + an	4	–36.0	1.6	–34.8	1.8	–16.1	1.5
	px + sp (+an)	2	–33.3	1.6	–34.3	2.0	–17.0	1.8
	an	3	–33.8	1.6	–35.5	1.8	–17.9	1.6
ELD–154–10	sp + px	2	–18.7	1.6	–19.3	2.1	–9.5	1.9
	an	6	–22.5	1.8	–29.8	2.3	–18.1	2.1
	an + w	3	–12.6	1.6	–12.7	1.9	–6.1	1.7
	sp + an	9	–30.9	1.7	–32.8	1.8	–16.7	1.6
	an + sp–frct	5	–8.6	1.7	–14.4	2.6	–10.0	2.5
	px	7	–16.0	1.6	–22.3	2.0	–13.9	1.8
	px	8	–17.8	1.7	–21.0	1.9	–11.8	1.7
EET–10–3	fo (+px)	1	–47.7	1.6	–45.5	2.6	–20.7	2.4
	sp	2	–50.3	1.6	–48.4	2.4	–22.3	2.2
ELD–154–60	fo	2	–41.9	1.6	–45.9	2.1	–24.1	1.9
	fo	4	–41.2	1.6	–45.5	2.0	–24.1	1.8
	px (+sp)	1	–35.1	1.6	–39.2	2.2	–20.9	2.0
	px (+fo)	3	–34.5	1.6	–39.9	1.9	–21.9	1.7
GRA–31–10	fo	1	–44.7	1.6	–46.9	1.9	–23.7	1.7
	sp	2	–46.9	1.6	–46.1	2.0	–21.7	1.8
	an (+px)	3	–45.4	1.6	–44.0	2.2	–20.4	2.1
PCA–16–5	fo	1	–44.2	1.6	–46.8	2.8	–23.8	2.6
	an + px	2	–41.2	1.6	–43.4	2.1	–22	1.9

*2σ errors calculated from analytical errors and average reproducibility on standards.
†Spots with ^{16}O contamination from Al-Mg analyses (see text).
Abbreviations: pts = polished thin section; GRA = Graves Nunataks; PCA = Pecora Escarpment; EET = Elephant Moraine; MET = Meteorite Hills; CAI = calcium–aluminum–rich inclusion; AOA = amoeboid olivine aggregate; MK = M. Kilgoure; UH = University of Hawai'i; number = Antarctic Meteorite Working Group designations; hib = hibonite; grs = grossite; pv = perovskite; mel = melilite; sp = spinel; px = pyroxene; an = anorthite; fo = forsterite; mt = metal; sec = secondary minerals [rim minerals]; anh = anhedral; euh = euhedral; pls = palisades; fl = fluffy; chd = chondrule; ign = igneous; fr = fragment; FG = fine=grained; A = similarities with type A inclusions; w = terrestrial weathering; frct = fracture.

The grossite-bearing melilite-rich CAI fragment GRA-17-7 has been previously measured for Mg-isotopic composition with the CAMECA ims 4f at the Physical Research Laboratory (India) using a pure ^{16}O primary ion beam for sputtering (Marhas *et al.*, 2001). It was subsequently re-polished with 1 μm diamond paste and re-coated. Although spots for oxygen isotope analysis have been chosen to be as far as possible from the previous ion probe pits, spot 1 could be artificially enriched in ^{16}O by the halo of a nearby ion probe pit (Table 5; Fig. 6b). To test this hypothesis, spot 3 was put deliberately close (a few microns away; Fig. 6b) from the previous pit. The oxygen-isotopic composition of melilite in spot 3 evolved during analysis from $\delta^{18}O \approx -80‰$ to about –40‰ with progressive sputtering by the Cs^+ beam. This experiment demonstrates that 10 to 20 μm halos corresponding to shallow ion implantation surrounding 5 μm pits can contribute significantly to ^{16}O contamination, and that it is difficult to quantitatively remove this contamination by light re-polishing of the sample. Moreover, such contaminated regions are difficult to detect (optically) following re-polishing and re-coating. These results show that for small phases in small CAIs, ion probe analyses using an ^{16}O primary beam should be preferentially done after O-isotope analysis to avoid possible contamination. Spot 2 measured with a smaller beam further away from the previous pits confirmed that the melilite, though ^{16}O-rich, does not exceed the lower end of the CAI trend ($\delta^{18}O$, $\delta^{17}O \approx -40‰$, $\Delta^{17}O = -23.7 \pm 1.5‰$). In spite of the significant differences in primary mineralogy and volatility among the other 21 CR CAIs and AOAs, they are all ^{16}O-rich ($\Delta^{17}O$ of hibonite, melilite, spinel, pyroxene, and anorthite less than –22‰) and isotopically homogeneous within 3–4‰ (Table 5; Figs. 15–17).

DISCUSSION

Our mineralogical observations suggest that CAIs and AOAs in CR chondrites largely escaped thermal metamorphism and low-temperature alteration which affected similar objects in the CV and CO carbonaceous chondrites and resulted in

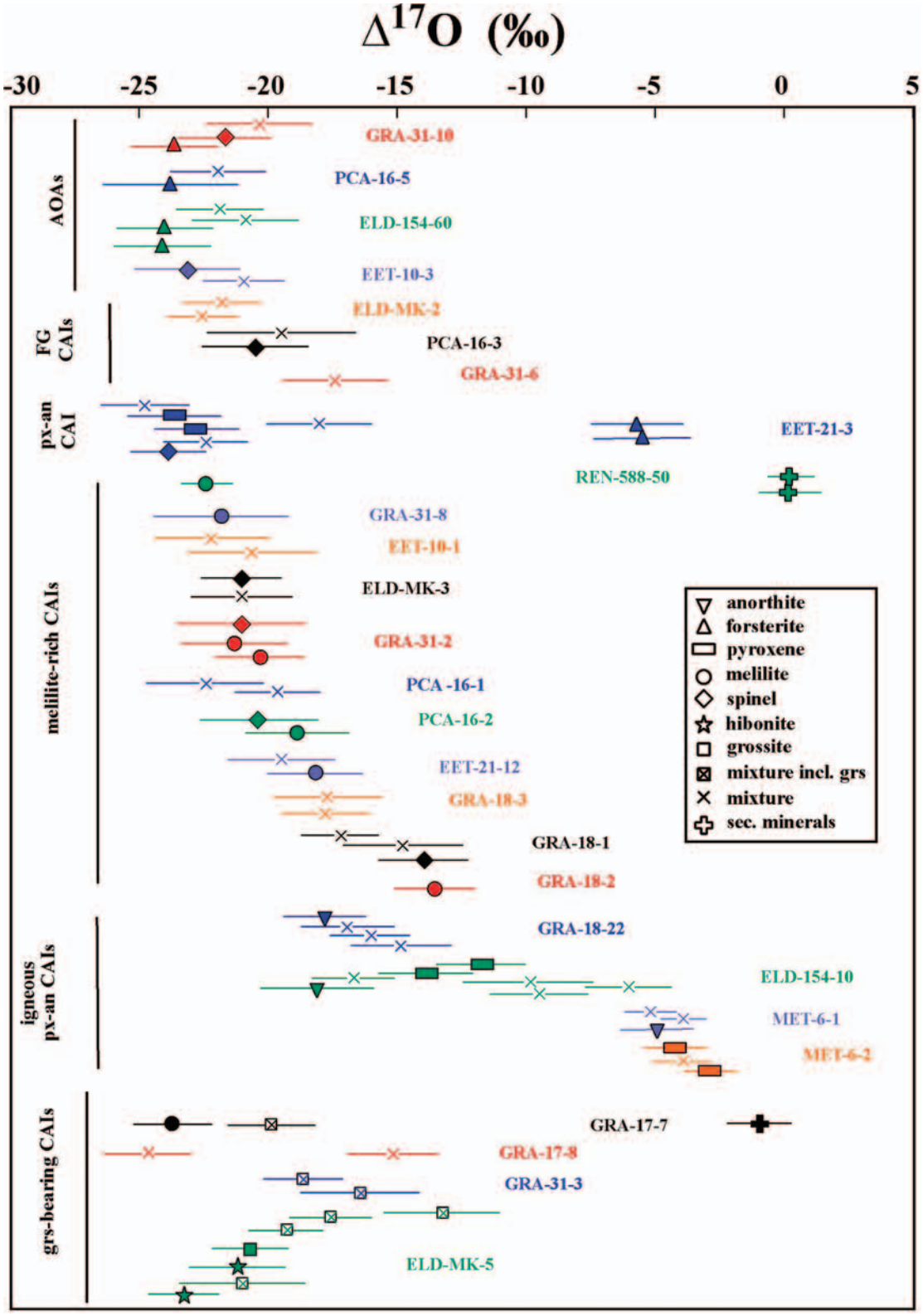

FIG. 16. $\Delta^{17}O$ of the CAIs and AOAs in CR chondrites. Pure mineral phases are distinguished from mixtures in the ion probe spot. Among the remarkable features, AOAs are uniformly enriched in ^{16}O ($\Delta^{17}O = -21‰$ down to $-25‰$), melilite-rich CAIs have uniform $\Delta^{17}O$, but spread from $-23‰$ up to $-13‰$, igneous pyroxene-anorthite CAIs are ^{16}O-depleted, and grossite-rich CAIs show some compositional heterogeneity. Errors are 2σ.

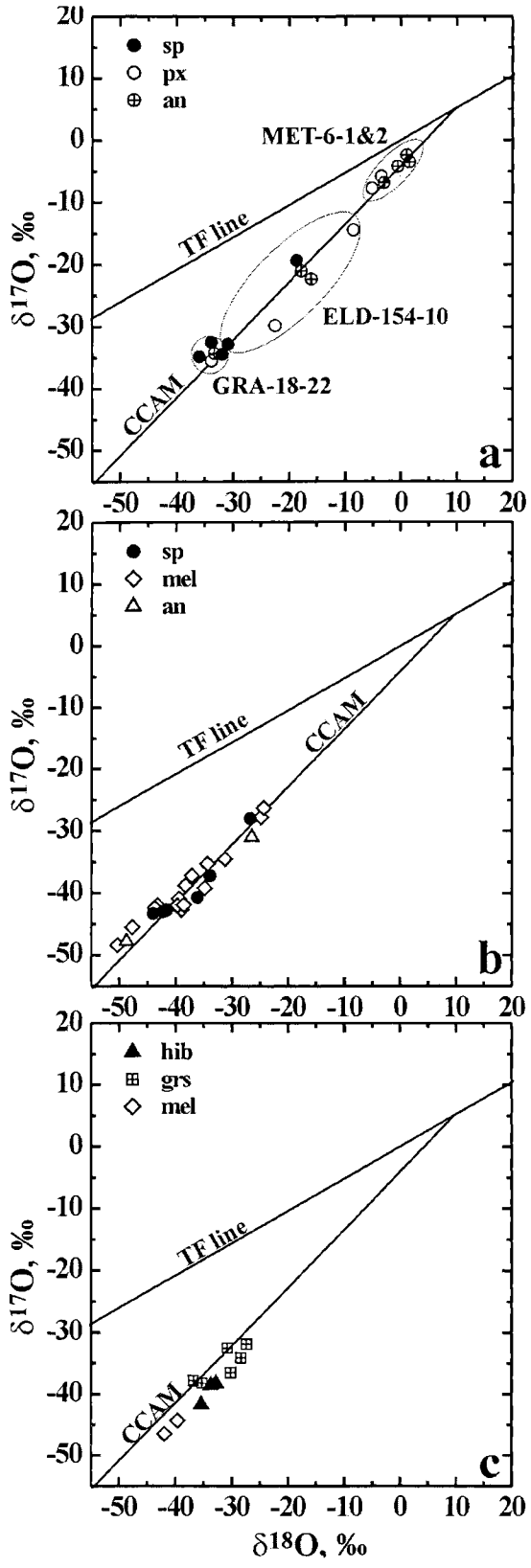

FIG. 17. Oxygen-isotopic composition of specific types of CAIs: igneous pyroxene-anorthite CAIs (a), melilite-rich CAIs (b) and grossite ± hibonite-rich CAIs (c).

formation of ferrous olivine, nepheline, sodalite, grossular, wollastonite, andradite, and enrichment of spinel and olivine in FeO (*e.g.*, MacPherson *et al.*, 1988; Russell *et al.*, 1998; Komatsu *et al.*, 2001). The low contents of FeO in spinel and olivine of the CR CAIs and AOAs suggests that these meteorites escaped even mild thermal metamorphism. This conclusion is consistent with the presence, in CR chondrites, of primitive FeNi-metal which did not experience exsolution into taenite and kamacite (Weisberg *et al.*, 1993). The general absence of secondary minerals in CR CAIs and AOAs is also consistent with a low degree of aqueous alteration of the Antarctic CR chondrites (Weisberg *et al.*, 1993); most of the CAIs studied here are from Antarctic meteorites. The only CAI studied in the moderately altered Renazzo consistently contains secondary minerals. No CAIs have been studied from the Al Rais meteorite, which experienced the highest degree of aqueous alteration among known CR chondrites (Weisberg *et al.*, 1993).

A Condensation Origin of CR Amoeboid Olivine Aggregates and Most Calcium-Aluminum-Rich Inclusion Protoliths

Given that most refractory phases in the CR chondrites are not substantially altered by aqueous activity on the parent body, we can infer that their isotopic compositions are determined by nebular processes. However, the inferences regarding nebular isotopic reservoirs depend on constraining the possibilities for CAI and AOA petrogenesis. For example, distinctly different conclusions can be reached with respect to oxygen isotopic fractionations between gaseous and solid phases in the solar nebula depending on the formation histories of CAIs. The AOAs in CR chondrites are texturally and mineralogically similar to those in the reduced CV chondrites (Komatsu *et al.*, 2001). Based on the porous aggregation textures of the CV AOAs and the similar estimated condensation temperatures (Petaev and Wood, 1998) of their primary minerals diopside (1323 K), forsterite (1318 K), and FeNi-metal (1290 K), it was concluded that the CV AOAs originated by gas–solid condensation, agglomeration, and annealing without substantial melting (Komatsu *et al.*, 2001). A similar conclusion can be reached for the CR AOAs based on the petrographic observations described above. However some melting might have taken place, although probably only to a small degree, as evidenced by the relatively compact textures of the AOAs and the heating experiments of olivine-anorthite mixtures by Komatsu *et al.* (2002). These experiments demonstrate that a small degree of melting of olivine and anorthite could result in the formation of Al-diopside of variable compositions which overgrows forsteritic olivine grains, as in the CR AOAs. This observation is in contrast to thermodynamic calculations which predict condensation of diopside prior to forsterite (Petaev and Wood, 1998). We conclude that the CR AOAs are aggregates of gas–solid condensate grains that experienced minor melting.

MacPherson and Huss (2000) used the bulk chemical compositions of CAIs (including bulk compositions of the CR CAIs published by Weber and Bischoff (1997)) and the calculated equilibrium condensation path from a gas of solar composition to argue that most CAI protoliths represent condensates rather than evaporative residues.

The mineralogical and textural evidence shows that the CR CAIs experienced a wide range of degrees of melting from essentially none in the fine-grained inclusions (Fig. 7) to nearly complete melting in the igneous CAIs (Figs. 2c, 9 and 10). Although the final melting episodes obscure the original mode of formation of many of the samples, it is likely that the CAI protoliths formed by gas–solid condensation. Note that this conclusion does not exclude partial volatilization of CAIs during melting and crystallization (Grossman *et al.*, 2000, 2002).

If the CR AOAs and CAIs originated as condensates, then based on the absence of low-Ca pyroxene associated with the AOAs and the depletion of both AOAs and CAIs in moderately volatile elements such as Mn, Cr, Na, K, and S, we can conclude that these objects were isolated (removed) from further reactions with ambient gas at high temperatures. An exception is given by the igneous pyroxene-anorthite CAIs which do show unusually high contents of moderately volatile elements, such as Cr in spinel and Na in melilite (see above).

Comparison of Calcium-Aluminum-Rich Inclusions from CR and Other Carbonaceous Chondrite Groups: Evidence for Multiplicity of Calcium-Aluminum-Rich Inclusion Formation

The CR clan was established by Weisberg *et al.* (1995) and includes four kinds of chondrites: (1) CR group, (2) CH group, (3) HH 237 and QUE 94411 paired with QUE 94627, and (4) Bencubbin, Gujba, and Weatherford. The term "clan" is defined as chondrites that have general chemical, mineralogical and isotopic similarities that suggest a petrogenetic kinship, but have petrologic and/or bulk chemical differences that invalidate a group relationship. In this section, we compare CAIs from the CR, CH, and QUE 94411, HH 237 carbonaceous chondrites (so far, no CAIs have been found in Bencubbin and Weatherford but two were reported recently in Gujba: a melilite-pyroxene-spinel inclusion (Weisberg *et al.*, 2002) and a pyroxene-spinel-olivine inclusion (Weisberg, pers. comm.)).

The CAIs in CH chondrites are generally tiny (<30 μm in diameter), compact, rounded and very refractory with grossite, hibonite, spinel, melilite, and Al-Ti-diopside as the major minerals. Most of the CH CAIs were probably melted (Kimura *et al.*, 1993; Sahijpal *et al.*, 1999). Anorthite-bearing CAIs are exceptionally rare and AOAs are absent (Grossman *et al.*, 1988; MacPherson *et al.*, 1989; Kimura *et al.*, 1993; Weber *et al.*, 1995; Sahijpal *et al.*, 1999). Most CH CAIs are surrounded by either a dual-layered rim (an interior melilite and an outer pyroxene) or a single layer of pyroxene; forsterite rims are very rare.

The CR CAIs are less refractory on average than those in CH chondrites: melilite-rich CAIs and AOAs are the dominant types of inclusions; secondary anorthite replacing melilite is fairly common. The Wark–Lovering rim sequence around CR CAIs consists of spinel, ±melilite, ±anorthite, and pyroxene; forsterite layers are rare (Weisberg and Prinz, 1990; Weber and Bischoff, 1997; Marhas *et al.*, 2001; this study).

The HH 237 and QUE 94411 CAIs are also less refractory on average than those in CH chondrites; but in contrast to the CR CAIs, those in HH 237 and QUE 94411 are predominantly pyroxene-rich and surrounded by monomineralic forsterite rims. Anorthite-bearing CAIs are very rare in these meteorites, as are AOAs (Krot *et al.*, 2001a).

The observed differences in the CAI mineralogy can be explained as a result of isolation (removal) of the CAIs from the nebular gas at various different temperatures (Weber and Bischoff, 1997; Krot *et al.*, 2001b). The very refractory nature and nearly complete absence of the relatively low-temperature condensates, such as anorthite and forsterite, in the CH CAIs may indicate that these inclusions were removed from the CAI-forming region(s) prior to condensation of these minerals. The less refractory nature of the CAIs in QUE 94411, HH 237 and CR chondrites, and the common presence of forsterite in and around CAIs in QUE 94411/HH 237 and secondary anorthite in CR CAIs, suggests that these inclusions persisted in contact with the gas in the CAI-forming region(s) to lower temperatures (~1300 K).

A comparison of CAIs from CR chondrites to those from other chondrite groups shows that most inclusion types existing in CR chondrites have similar counterparts in at least one of the other carbonaceous, enstatite or ordinary chondrite groups (*e.g.*, Table 11 in Krot *et al.*, 2001a). For example, most of the melilite-rich inclusions observed in CR chondrites are similar to fluffy type A inclusions (FTA) or compact type A inclusions in CV or CO chondrites (or seem to be fragments of such inclusions; Table 1). Grossite-rich inclusions in CR chondrites are mineralogically similar to those in CH chondrites (Weber *et al.*, 1995), but are less abundant. Fine-grained spinel-rich inclusions in CR chondrites are mineralogically similar to those in other chondrite groups, but they are neither altered (compared to fine-grained CAIs in CM, CV or CO chondrites) nor concentrically zoned (compared to fine-grained CAIs in CV3 chondrites). AOAs in CR chondrites are mineralogically similar to those in other carbonaceous chondrites (*e.g.*, Hiyagon and Hashimoto, 1999; Komatsu *et al.*, 2001). The igneous pyroxene-anorthite CAIs are mineralogically similar to type B CAIs in CV chondrites, but they are smaller and less refractory than the latter. Melilite is notably far less abundant than in type B CAIs where it is often the major phase.

At the same time, several CAI types described in other carbonaceous chondrite groups have not been observed in CR chondrites yet. For example, spinel-pyroxene spherules, commonly found in CH chondrites (Krot *et al.*, 2001b), are absent in CR chondrites. Coarse-grained forsterite-bearing

CAIs have been reported only in CV (*e.g.*, Clayton *et al.*, 1984) and CB (Krot *et al.*, 2001a) chondrites. Platy hibonites (PLACs) and spinel-hibonite spherules (SHIBs) are common only in CM chondrites (Ireland, 1988).

Based on these observations, we infer that although CR CAIs have counterparts in other chondrite groups, each chondrite group has a distinct population of CAIs. If CAIs formed in a restricted region of the solar nebula, as has been recently argued (Shu *et al.*, 1996, 1997, 2001; McKeegan *et al.*, 1998; Krot *et al.*, 2002), these observations may indicate that there were multiple episodes of CAI formation in the solar nebula, each characterized by a distinct set of physical-chemical conditions (*e.g.*, dust/gas ratio, peak heating temperature, cooling rate, ambient temperature, isolation temperature, number of recyclings). The preservation of distinctive populations of CAIs then requires transport out of this hot subregion(s) of the nebula and fairly rapid accretion into larger bodies that, ultimately, could grow to become the parent asteroids of the chondrites.

The isotopic evidence also points to the possibility of episodic CAI formation in a restricted region of the solar nebula (*i.e.*, a region not generally characteristic of the formation regions of most chondrules or of the chondrite accretion regions (presumably near the asteroid belt)). For example, the general similarity of oxygen-isotopic compositions of most CAIs and AOAs, and their large difference in ^{16}O enrichment with essentially all other materials in chondrites, has been put forth as an argument for formation of CAIs (or their precursors) in a restricted locale, probably near the forming protosun (*e.g.*, McKeegan *et al.*, 1998). That some CAIs, and most if not all AOAs, must have formed by condensation from an ^{16}O-rich gas (Krot *et al.*, 2002) further supports this interpretation (also, see below). However, there do exist important isotopic differences between CAIs from different chondrite groups that complicate this picture. These differences are present in both stable (*e.g.*, oxygen) and radiogenic (*e.g.*, ^{26}Al) isotope systems. Our data show that even within the CR clan, oxygen-isotopic distributions form distinct populations among CAIs. Additionally, the variation of isotopic compositions of melilite shows that there must be different histories for CAIs from different chondrite groups. Furthermore, whereas most CR CAIs show excess of ^{26}Mg ($^{26}Mg^*$) corresponding to a canonical ($^{26}Al/^{27}Al$) ratio of 5×10^{-5} (Marhas *et al.*, 2001), most grossite-rich and hibonite-rich CAIs in CH chondrites and PLAC hibonites in CM chondrites lack detectable $^{26}Mg^*$ (Ireland, 1988; Ireland and Fegley, 2000; Weber *et al.*, 1995).

Oxygen-16-Rich Gaseous Reservoir in the Solar Nebula

Forsterite, spinel, anorthite, and pyroxene in the CR AOAs have nearly identical ^{16}O-rich isotopic compositions (Table 5; Figs. 15a and 16). These observations, together with the condensation origin of forsterite, spinel and anorthite in AOAs (Komatsu *et al.*, 2001), suggest that AOAs formed in an ^{16}O-enriched gaseous reservoir (Krot *et al.*, 2002). If pyroxene in AOAs resulted from a small degree of melting of forsterite and anorthite (Komatsu *et al.*, 2002), this melting must have occurred in the same region characterized by ^{16}O-enriched gas.

Primary minerals in most of the CR CAIs are enriched in ^{16}O to the same level as observed in the CR AOAs ($\Delta^{17}O$ of hibonite, melilite, spinel, pyroxene, and anorthite less than –22‰) and isotopically homogeneous within 3–4‰ (Table 5; Figs. 15b and 16). If, as suggested above, the CR CAI protoliths had a condensation origin (Yoneda and Grossman, 1995; MacPherson and Huss, 2000; Grossman *et al.*, 2002), then it is likely that CAIs and AOAs formed in the same ^{16}O-enriched gaseous reservoir.

The existence of an ^{16}O-rich gaseous reservoir in the protosolar nebula has been recently inferred from the discovery of ^{16}O-rich corundum, hibonite, and forsterite condensates in the CM and CV CAIs and AOAs (Hiyagon and Hashimoto, 1999; Krot *et al.*, 2002; Simon *et al.*, 2002). Corundum and hibonite are the most refractory condensates, whereas forsterite and the reaction product anorthite, which replaces melilite, are the least refractory. Since all these minerals have ^{16}O-rich isotopic compositions (Hiyagon and Hashimoto, 1999; Krot *et al.*, 2002; Simon *et al.*, 2002, this study), we infer that the ^{16}O-enriched gaseous reservoir in the CAI-forming region(s) prevailed through a large temperature interval during CAI formation.

Effect of Remelting on Oxygen-Isotopic Compositions of Calcium-Aluminum-Rich Inclusions

In spite of the oxygen-isotopic homogeneity of individual CAIs, the compositions of the CR CAIs spread almost continuously over a wide range from $\Delta^{17}O = -3‰$ to $\Delta^{17}O = -24‰$ (Fig. 15b). There appears to be a correlation between oxygen-isotopic compositions of the CR CAIs and textural type: most (six out of eight) CAIs which have igneous textures are ^{16}O-poor ($\Delta^{17}O = -18‰$ to $-3‰$), whereas most other CAIs are ^{16}O-rich. The ^{16}O-poor CAIs (Table 5; Fig. 17a) include four pyroxene-anorthite-rich inclusions with lath-shaped anorthite (ELD-154-10, MET-6-1, MET-6-2, and GRA-18-22; Figs. 9 and 10) and two compact melilite-rich CAIs with euhedral spinel grains (GRA-18-2 and GRA-18-3; Fig. 2c). For two ^{16}O-poor melilite-rich CAIs (GRA-18-1 and EET-21-12), textural observations do not allow us to distinguish between igneous *vs.* non-igneous (*i.e.*, condensation and sintering) origin of the inclusions. We note however that anorthite in the CAI GRA-18-1 replaces melilite and must have a condensation origin (Fig. 4a,b). With the exception of ELD-154-10, the igneous CAIs are uniformly ^{16}O-poor (*i.e.*, $\Delta^{17}O$ of spinel, pyroxene, melilite, and anorthite in an individual CAI are similar within 3‰). The two ^{16}O-rich CAIs, GRA-17-7 and GRA-17-8, for which we have inferred possibly large degrees of melting may, in fact, be fragments of a single inclusion.

It is likely that the ^{16}O-poor isotopic compositions of the igneous CR CAIs resulted from melting of originally ^{16}O-rich

CAIs in a gas with a relatively ^{16}O-depleted composition (*i.e.*, somewhere near or above the TF line). Such CAI melts would have achieved nearly complete oxygen isotopic exchange with the gas relatively quickly (Ryerson and McKeegan, 1994; Yu *et al.*, 1995) accounting for their homogeneity. Only ELD-154-10, which may have experienced partial melting (as indicated by the presence of two melilites, $Åk_{17}$ and $Åk_{77}$), would have recorded incomplete isotopic exchange, or continued exchange following initial crystallization. The large range in $\Delta^{17}O$ among the various ^{16}O-poor CAIs could, in principle, reflect either a variable degree of exchange between the CAI melts and the gaseous reservoir or that the exchange occurred in gaseous reservoirs of different oxygen-isotopic compositions. The latter seems more likely; otherwise a greater degree of intra-CAI heterogeneity would be expected. An anorthite of probable condensation origin in GRA-18-1 that is relatively ^{16}O-poor is also best explained as indicating the existence of a relatively ^{16}O-depleted gas at some time in the region where this CAI formed.

The ^{16}O-poor pyroxene-anorthite-rich CAIs in CR chondrites are less refractory than type B CAIs in CV chondrites: (1) pyroxene is relatively Ti-poor (Table 4), (2) melilite is Åk-rich and contains traces of Na (Table 3), and (3) spinel is Cr-bearing. Therefore, they must have been melted at a relatively low ambient temperature (at or below condensation temperatures of moderately volatile elements such as Cr and Na) compared to the most refractory CAIs of the CR-clan. This melting took place in an environment that was isotopically similar to most components of chondrites; thus it is reasonable to assume that the predominant gas in this environment is more characteristic of "the solar nebula" than the gas from which most CAI precursors condensed.

Effects of Alteration on Oxygen Isotopes

The ensemble of all CR CAIs and AOAs defines a best-fit mixing line ($\delta^{17}O = 0.956 \pm 0.025 \times \delta^{18}O - 4.01 \pm 0.34$) that is identical within error to the CCAM line ($\delta^{17}O = 0.945 \times \delta^{18}O - 4.17$), defined originally by CAIs from Allende (Clayton *et al.*, 1977). This mixing line is inconsistent with a line of slope 1.00 proposed recently by Young and Russell (1998) based on O-isotopic compositions of primary minerals in one relatively unaltered type B CAI from Allende and observed in other populations of mineralogically unaltered CAIs (McKeegan and Leshin, 2001 and references therein). However, the relatively ^{16}O-poor igneous CAIs strongly control the best-fit line through the CR CAI data points, making the interpretation of the deviation of the CR data from the Young and Russell line problematic. We have argued above that these CAIs are best explained as having equilibrated isotopically with a relatively ^{16}O-poor gas; however, it is also conceivable that these CAIs may have suffered mass-dependent fractionation of oxygen isotopes during evaporation from a melt. Additionally, if a prior generation of low-temperature secondary minerals were present in the protolith, the petrologic evidence was destroyed during the last melting event. Thus, it is difficult to use these CAIs to comment on the relevance of the CR data to the Young and Russell hypothesis. Nevertheless, the presence of alteration phases in a minority of CR CAIs does offer an opportunity to assess the effects of aqueous alteration in these objects with regard to their oxygen-isotopic compositions.

Two melilite-rich CAIs (GRA-17-7 and REN-588-50) contain secondary phases indicating that they experienced post-crystallization alteration (Figs. 5 and 6). The secondary phases (phyllosilicates (?), nepheline (?), sodalite (?)) are ^{16}O-poor and plot along the TF line. We note that alteration phases in REN-588-50 are close to (within error of) the value of the hydrous matrix of Renazzo determined by Clayton and Mayeda (1999). In addition, Renazzo is a fall, which suggests that these alteration phases probably do not result from terrestrial weathering. In spite of the observed oxygen-isotopic compositions of the secondary phases, melilite of the host CAIs is ^{16}O-rich ($\Delta^{17}O < -22‰$). Thus, there was no appreciable oxygen-isotopic exchange between the CR CAIs and the ^{16}O-poor fluid responsible for the alteration.

It has been recently suggested that CAIs and AOAs in CO and CV chondrites experienced oxygen isotope exchange during iron-alkali-metasomatic alteration (Wasson *et al.*, 2001; Fagan *et al.*, 2002). Since the secondary minerals produced during this alteration (*e.g.*, ferrous olivine, hedenbergite, wollastonite, andradite, and grossular) are different from those observed in the CR CAIs, a different type of alteration might have affected CR CAIs. The effect of fluid circulations on melilite isotopic composition remains unclear and requires further studies.

In the CR CAIs ELD-MK-5 and GRA-17-7, grossite is systematically depleted in ^{16}O compared to coexisting hibonite or melilite (Table 5; Fig. 17c). Hiyagon (2000) reported that ^{16}O-poor grossite ($\Delta^{17}O \approx -3‰$ to 0‰) coexists with ^{16}O-rich hibonite and melilite in a CAI from the CO3 chondrite Yamato 81020. These observations may indicate that grossite is more susceptible to oxygen-isotopic exchange than even melilite.

CONCLUSIONS

From our textural, mineralogical, and isotopic observations, we can postulate a scenario for formation of the CR inclusions that is consistent with what is known from CAIs in the other chondrite groups. The CR AOA and CAI protoliths have probably initially formed by condensation from an ^{16}O-rich gaseous reservoir at temperatures ranging from the condensation temperature of hibonite to that of forsterite. Subsequently most of the CR AOAs and CAIs experienced sintering or some melting in the same ^{16}O-rich reservoir. Some of the CAIs (the igneous pyroxene-anorthite-rich CAIs) were subsequently extensively melted in the presence of an ^{16}O-depleted nebular gas environment at lower ambient temperature. The CR CAIs do not show significant isotopic heterogeneity within an

individual inclusion suggesting that the isotopic composition of each inclusion is determined by equilibrium with the high-temperature gas with which it last reacted. Thus, the non-mass-dependent oxygen-isotopic variations among the CAIs must reflect variability of the isotopic composition of the gaseous reservoirs in which the formation and subsequent processing of the inclusions took place. The variability in volatility of different CAIs requires isolation from the hot nebular gas at different temperatures. Together with the observation of different populations of CAIs in different chondrite groups, this suggests that CAI formation occurred in multiple episodes. In such a model, the isotopic heterogeneity between melilite and the other primary minerals that exists in other chondrite groups (*e.g.*, CV) reflects secondary processing of originally ^{16}O-rich materials. Such processing may have occurred in more than one type of environment (*e.g.*, asteroidal or nebular). However, our data suggest that aqueous alteration of CR parent bodies did not affect the oxygen-isotopic composition of melilite.

In an x-wind model of the protosun environment (Shu *et al.*, 1996, 1997, 2001), the above scenario implies an ^{16}O-rich gaseous reservoir should be located in a restricted region close to the Sun, where CAI protoliths formed by gas–solid condensation. Different mechanisms can be invoked to explain the existence of this reservoir: chemical reactions associated with mass-independent fractionation (*e.g.*, Thiemens and Heidenreich, 1983; Thiemens, 1999), evaporation of ^{16}O-rich presolar dust (Scott and Krot, 2001) or photochemical self-shielding (*e.g.*, Navon and Wasserburg, 1985; Clayton, 2002). Multiple episodes of CAI formation (*e.g.*, cycles of condensation, evaporation and/or melting) would in that case be associated with variability of the energetic environment near the protosun (*e.g.*, x-ray flares, magnetic reconnection events), coupled with episodic removal of CAI protoliths from that hot region by x-winds. Later events affecting the CAI protoliths (*e.g.*, melting, alteration) could take place further away from the Sun in a region with gaseous environment of heavier oxygen-isotopic composition, characteristic of the other components of chondrites. This scenario may, of course, not offer a unique explanation for all the mineralogical and isotopic data, but it has the distinct advantage of providing a natural mechanism, thought to occur during the formation of most low-mass stars (Feigelson and Montmerle, 1999), for allowing transport of solid particles between two gaseous reservoirs that are apparently distinct in isotopic composition and temperature.

Acknowledgments–We thank the Antarctic Meteorite Working Group (NASA, Johnson Space Center), Michael K. Weisberg (American Museum of Natural History, New York), Addi Bischoff (Institut für Planetologie, Münster), Ansgar Greshake (Institut für Mineralogie, Humboldt Universität, Berlin) and Marvin Kilgoure for providing polished thin sections of the meteorites studied. We thank Chris Coath and George Jarzebinski at UCLA for ion probe help and maintenance, and A. Meibom, E. R. D. Scott, S. S. Russell, M. K. Weisberg, and J. R. Lyons for helpful discussions. We would like to thank S. Ross Taylor for the editorial work and Sara S. Russell and Michael K. Weisberg for thoughtful reviews. This work was supported by NASA grants NAG5-4704 (K. D. McKeegan, P. I.), NAG5-10610 (A. N. Krot, P. I.) and NAG5-11591 (K. Keil, P. I.). The UCLA ion microprobe laboratory is partially supported by a grant from the NSF Instrumentation and Facilities Program. This is Hawaii Institute of Geophysics and Planetology publication No. 1248 and School of Ocean and Earth Science and Technology publication No. 6060.

Editorial handling: S. R. Taylor

REFERENCES

CLAYTON R. N. (1993) Oxygen isotopes in meteorites. *Ann. Rev. Earth Planet. Sci.* **21**, 115–149.

CLAYTON R. N. (2002) Photochemical self-shielding in the solar nebula (abstract). *Lunar Planet. Sci.* **33**, #1326, Lunar and Planetary Institute, Houston, Texas, USA (CD-ROM).

CLAYTON R. N. AND MAYEDA T. K. (1978) Genetic relations between iron and stony meteorites. *Earth Planet. Sci. Lett.* **40**, 168–174.

CLAYTON R. N. AND MAYEDA T. K. (1999) Oxygen isotope studies of carbonaceous chondrites. *Geochim. Cosmochim. Acta* **63**, 2089–2104.

CLAYTON R. N., ONUMA N., GROSSMAN L. AND MAYEDA T. K. (1977) Distribution of the presolar component in Allende and other carbonaceous chondrites. *Earth Planet. Sci. Lett.* **34**, 209–224.

CLAYTON R. N., MACPHERSON G. J., HUTCHEON I. D., DAVIS A. M., GROSSMAN L., MAYEDA T. K., MOLINI-VELSKO C. AND ALLEN J. M. (1984) Two forsterite-bearing FUN inclusions in the Allende meteorite. *Geochim. Cosmochim. Acta* **48**, 535–548.

FAGAN T. J., MCKEEGAN K. D., KROT A. N. AND KEIL K. (2001) Calcium-aluminum-rich inclusions in enstatite chondrites (II): Oxygen isotopes. *Meteorit. Planet. Sci.* **36**, 223–230.

FAGAN T. J., YURIMOTO H., KROT A. N. AND KEIL K. (2002) Constraints on oxygen isotopic evolution from an amoeboid olivine aggregate and Ca, Al-rich inclusion from the CV3 Efremovka (abstract). *Lunar. Planet. Sci.* **33**, #1507, Lunar and Planetary Institute, Houston, Texas, USA (CD-ROM).

FEIGELSON E. D. AND MONTMERLE T. (1999) High-energy processes in young stellar objects. *Ann. Rev. Astron. Astrophys.* **37**, 363–408.

GROSSMAN L. (1980) Refractory inclusions in the Allende meteorite. *Ann. Rev. Earth Planet. Sci.* **8**, 559–608.

GROSSMAN L., EBEL D. S., SIMON S. B., DAVIS A. M., RICHTER F. M. AND PARSAD N. M. (2000) Major element chemical and isotopic compositions of refractory inclusions in C3 chondrites; the separate roles of condensation and evaporation. *Geochim. Cosmochim. Acta* **64**, 2879–2894.

GROSSMAN L., EBEL D. S. AND SIMON S. B. (2002) Formation of refractory inclusions by evaporation of condensate precursors. *Geochim. Cosmochim. Acta* **66**, 145–161.

GROSSMAN J. N., RUBIN A. E. AND MACPHERSON G. J. (1988) ALH 85085; a unique volatile-poor carbonaceous chondrite with possible implications for nebular fractionation processes. *Earth Planet. Sci. Lett.* **91**, 33–54.

GUAN Y., MCKEEGAN K. D. AND MACPHERSON G. J. (2000) Oxygen isotopes in calcium-aluminum-rich inclusions from enstatite chondrites: New evidence for a single CAI source in the solar nebula. *Earth Planet. Sci. Lett.* **181**, 271–277.

HIYAGON H. (2000) Highly heterogeneous distribution of oxygen isotopes in a grossite-bearing inclusion from Yamato 81020 (CO3) chondrite (abstract). *Meteorit. Planet. Sci.* **35 (Suppl.)**, A75.

HIYAGON H. AND HASHIMOTO A. (1999) ^{16}O excesses in olivine inclusions in Yamato-86009 and Murchison chondrites and their relation to CAIs. *Science* **283**, 828–830.

IRELAND T. R. (1988) Correlated morphological, chemical, and isotopic characteristics of hibonites from the Murchison carbonaceous chondrite. *Geochim. Cosmochim. Acta* **52**, 2827–2839.

IRELAND T. R. AND FEGLEY B., JR. (2000) The solar system's earliest chemistry: Systematics of refractory inclusions. *Intl. Geol. Rev.* **42**, 865–894.

IRELAND T. R., FAHEY A. J. AND ZINNER E. K. (1991) Hibonite-bearing microspherules: A new type of refractory inclusions with large isotopic anomalies. *Geochim. Cosmochim. Acta* **55**, 367–379.

KIMURA M., EL GORESY A., PALME H. AND ZINNER E. (1993) Ca-, Al-rich inclusions in the unique chondrite ALH 85085: Petrology, chemistry, and isotopic compositions. *Geochim. Cosmochim. Acta* **57**, 2329–2359.

KOMATSU M., KROT A. N., PETAEV M. I., ULYANOV A. A., KEIL K. AND MIYAMOTO M. (2001) Mineralogy and petrography of amoeboid olivine aggregates from the reduced CV3 chondrites Efremovka, Leoville and Vigarano: Products of nebular condensation, accretion and annealing. *Meteorit. Planet. Sci.* **36**, 629–641.

KOMATSU M., MIYAMOTO M., MIKOUCHI T., KROT A. N. AND KEIL K. (2002) Heating experiments of olivine-anorthite mixtures: Clues to understanding the textural relationships among olivine, Al-diopside and anorthite in amoeboid olivine aggregates (abstract). *Lunar Planet. Sci.* **33**, #1258, Lunar and Planetary Institute, Houston, Texas, USA (CD-ROM).

KROT A. N., MCKEEGAN K. D., RUSSELL S. S., MEIBOM A., WEISBERG M. K., ZIPFEL J., KROT T. V., FAGAN T. J. AND KEIL K. (2001a) Refractory calcium-aluminum-rich inclusions and aluminum-diopside-rich chondrules in the metal-rich chondrites Hammadah al Hamra 237 and Queen Alexandra Range 94411. *Meteorit. Planet. Sci.* **36**, 1189–1216.

KROT A. N., MEIBOM A., WEISBERG M. K. AND KEIL K. (2001b) The CR chondrite clan: Implications for early solar system processes. *Meteorit. Planet. Sci.* **37**, 1451–1490.

KROT A. N., MCKEEGAN K. D., LESHIN L. A., MACPHERSON G. J. AND SCOTT E. R. D. (2002) Existence of an ^{16}O-rich gaseous reservoir in the solar nebula. *Science* **295**, 1051–1054.

LESHIN L. A., MCKEEGAN K. D. AND BENEDIX G. K. (2000) Oxygen isotope geochemistry of olivine from carbonaceous chondrites (abstract). *Lunar Planet. Sci.* **31**, #1918, Lunar and Planetary Institute, Houston, Texas, USA (CD-ROM).

MACPHERSON G. J. AND HUSS G. R. (2000) Convergent evolution of CAIs and chondrules: Evidence from bulk compositions and a cosmochemical phase diagram (abstract). *Lunar Planet. Sci.* **31**, #1796, Lunar and Planetary Institute, Houston, Texas, USA (CD-ROM).

MACPHERSON G. J., WARK D. A. AND ARMSTRONG J. T. (1988) Primitive material surviving in chondrites: Refractory inclusions. In *Meteorites and the Early Solar System* (eds. J. F. Kerridge and M. S. Matthews), pp. 746–807. Univ. Arizona Press, Tucson, Arizona, USA.

MACPHERSON G. J., DAVIS A. M. AND GROSSMAN J. N. (1989) Refractory inclusions in the unique chondrite ALH 85085 (abstract). *Meteoritics* **24**, 297.

MARHAS K. K., KROT A. N. AND GOSWAMI J. N. (2001) Al-Mg isotopic systematics in CAIs from CR chondrites (abstract). *Meteorit. Planet. Sci.* **36 (Suppl.)**, A121–A122.

MCKEEGAN K. D. AND LESHIN L. A. (2001) Stable isotope variations in extraterrestrial materials. In *Stable Isotope Geochemistry* (eds. J. W. Valley and D. R. Cole), pp. 279–378. Mineral. Soc. Am., Washington, D.C., USA.

MCKEEGAN K. D., LESHIN L. A., RUSSELL S. S. AND MACPHERSON G. J. (1998) Oxygen isotopic abundances in calcium-aluminum-rich inclusions from ordinary chondrites: Implications for nebular heterogeneity. *Science* **280**, 414–417.

NAVON O. AND WASSERBURG G. J. (1985) Self-shielding in O_2—A possible explanation for oxygen isotopic anomalies in meteorites? *Earth Planet. Sci. Lett.* **73**, 1–16.

PETAEV M. I. AND WOOD J. A. (1998) The condensation with partial isolation (CWPI) model of condensation in the solar nebula. *Meteorit. Planet. Sci.* **33**, 1123–1137.

RUSSELL S. S., HUSS G. R., FAHEY A. J., GREENWOOD R. C., HUTCHISON R. AND WASSERBURG G. J. (1998) An isotopic and petrologic study of calcium-aluminum-rich inclusions from CO3 meteorites. *Geochim. Cosmochim. Acta* **62**, 689–714.

RYERSON F. J. AND MCKEEGAN K. D. (1994) Determination of oxygen self-diffusion in åkermanite, anorthite, diopside and spinel: Implications for oxygen isotopic anomalies and the thermal histories of Ca-Al-rich inclusions. *Geochim. Cosmochim. Acta* **58**, 3713–3734.

SAHIJPAL S., MCKEEGAN K. D., KROT A. N., WEBER D. AND ULYANOV A. A. (1999) Oxygen-isotopic compositions of calcium-aluminum-rich inclusions from the CH chondrites Acfer 182 and Patuxent Range 91546 (abstract). *Meteorit. Planet. Sci.* **34 (Suppl.)**, A101.

SCOTT E. R. D. AND KROT A. N. (2001) Oxygen isotopic compositions and origins of calcium-aluminum-rich inclusions and chondrules. *Meteorit. Planet. Sci.* **36**, 1307–1319.

SHU F. H., SHANG H. AND LEE T. (1996) Toward an astrophysical theory of chondrites. *Science* **271**, 1545–1552.

SHU F. H., SHANG H., GLASSGOLD A. E. AND LEE T. (1997) X-rays and fluctuating x-winds from protostars. *Science* **277**, 1475–1479.

SHU F. H., SHANG H., GOUNELLE M. AND GLASSGOLD A. E. (2001) The origin of chondrules and refractory inclusions in chondritic meteorites. *Astrophys. J.* **548**, 1029–1050.

SIMON S. B., MCKEEGAN K. D., EBEL D. S. AND GROSSMAN L. (2000) Complexly zoned chromium-aluminum spinel found *in situ* in the Allende meteorite. *Meteorit. Planet. Sci.* **35**, 215–227.

SIMON S. B., DAVIS A. M., GROSSMAN L. AND MCKEEGAN K. D. (2002) A hibonite-corundum inclusion from Murchison: A first-generation condensate from the solar nebula. *Meteorit. Planet. Sci.* **37**, 533–548.

THIEMENS M. H. (1999) Mass-independent isotope effects in planetary atmospheres and the early solar system. *Science* **283**, 341–345.

THIEMENS M. H. AND HEIDENREICH J. E. (1983) The mass-independent fractionation of oxygen: A novel isotope effect and its possible cosmochemical implications. *Science* **219**, 1073–1075.

WASSON J. T., YURIMOTO H. AND RUSSELL S. S. (2001) ^{16}O-rich melilite in CO3 chondrites; possible formation of common ^{16}O-poor melilite by aqueous alteration. *Geochim. Cosmochim. Acta* **65**, 4539–4549.

WEBER D. AND BISCHOFF A. (1997) Refractory inclusions in the CR chondrite Acfer 059—El Djouf 001: Petrology, chemical composition, and relationship to inclusion populations in other types of carbonaceous chondrites. *Chem. Erde* **57**, 1–24.

WEBER D., ZINNER E. AND BISCHOFF A. (1995) Trace element abundances and magnesium, calcium, and titanium isotopic compositions of grossite-containing inclusions from the carbonaceous chondrite Acfer 182. *Geochim. Cosmochim. Acta* **59**, 803–823.

WEISBERG M. K. AND PRINZ M. (1990) Refractory inclusions in CR2 (Renazzo-type) chondrites (abstract). *Lunar Planet. Sci.* **21**, 1315–1316.

WEISBERG M. K., PRINZ M., CLAYTON R. N. AND MAYEDA T. K. (1993) The CR (Renazzo-type) carbonaceous chondrite group and its implications. *Geochim. Cosmochim. Acta* **57**, 1567–1586.

WEISBERG M. K., PRINZ M., CLAYTON R. N., MAYEDA T. K., GRADY M. M. AND PILLINGER C. T. (1995) The CR chondrite clan. *Proc. NIPR Symp. Antarct. Meteorites* **8**, 11–32.

WEISBERG M. K., PRINZ M., CLAYTON R. N., MAYEDA T. K., SUGIURA N., ZASHU S. AND EBIHARA M. (2001) A new metal-rich chondrite grouplet. *Meteorit. Planet. Sci.* **36**, 401–418.

WEISBERG M. K., BOESENBERG J. S. AND EBEL D. S. (2002) Gujba and the origin of the Bencubbin-like (CB) chondrites (abstract). *Lunar Planet. Sci.* **33**, #1551, Lunar and Planetary Institute, Houston, Texas, USA (CD-ROM).

YONEDA S. AND GROSSMAN L. (1995) Condensation of CaO-MgO-Al_2O_3-SiO_2 liquids from cosmic gases. *Geochim. Cosmochim. Acta* **59**, 3413–3444.

YOUNG E. D. AND RUSSELL S. S. (1998) Oxygen reservoirs in the early solar nebula inferred from an Allende CAI. *Science* **282**, 452–455.

YOUNG E. D., ASH R. D., ENGLAND P. AND RUMBLE D., III (1999) Fluid flow in chondritic parent bodies; deciphering the compositions of planetesimals. *Science* **286**, 1331–1335.

YU Y., HEWINS R. H., MAYEDA T. K. AND CLAYTON R. N. (1995) Experimental study of high temperature oxygen isotope exchange during chondrule formation. *Geochim. Cosmochim. Acta* **59**, 2095–2104.

YURIMOTO H., ITO M. AND NAGASAWA H. (1998) Oxygen isotope exchange between refractory inclusion in Allende and solar nebula gas. *Science* **282**, 1874–1877.